# Sentinel-MSI and Landsat-OLI Data Quality Characterization for High Temporal Frequency Monitoring of Soil Salinity Dynamic in an Arid Landscape

A. Bannari, N. Hameid, A. Abuelgasim and A. El-Battay

***Abstract* - The data collection with Multi Spectral Instrument (MSI) onboard Sentinel-2 satellites and the Operational Land Imager (OLI) installed on Landsat-8 satellite enhance significantly the Earth observation and monitoring with medium spatial resolutions and very high temporal frequency. However, although these instruments are designed to be similar, they have different spectral, spatial and radiometric resolutions. Moreover, relative spectral response profiles characterizing the filters responsivities of the both instruments are not identical between the homologous bands, so some differences are probably expected in the recorded land-surface reflectance values and, therefore, their data probably cannot be reliably used together. This paper analyse and compare the difference between the reflectance in the homologous spectral bands of MSI and OLI sensors, visible-near-infrared (VNIR) and shortwave infrared (SWIR), for high temporal frequency monitoring of soil salinity dynamic in an arid landscapes. In addition, their conversion in term of *Soil Salinity and Sodicity Index* (SSSI) and in term of *Semi-Empirical Predictive Model* (SEPM) for soil salinity mapping were compared, and their sensor differences were quantified. To achieve these, analyses were performed on simulated data and on two pairs of images acquired over the same area in July 2015 and August 2017 with one day difference between each pair. For simulated data, a field survey was organized and 160 soil samples were collected with various degrees of soil salinity classes (i.e., extreme, very high, high, moderate, low, and non-saline). The bidirectional reflectance factor was measured above each soil sample in a Goniometric-Laboratory using an *Analytical Spectral Devices* (ASD) FieldSpec-4 Hi-Res (high resolution) spectroradiometer. Then, these measurements were resampled and convolved in the solar-reflective bands of SMI and OLI using the *Canadian Modified Simulation of a Satellite Signal in the Solar Spectrum* (CAM5S) radiative transfer code and the relative spectral response profiles characterizing the filters of these instruments. Furthermore, the used pairs of images were not cloudy, or cirrus contaminated, and without shadow effects. They were radiometrically and atmospherically corrected, and the differences related to *Bidirectional Reflectance Distribution Function* (BRDF) were normalized. To generate data for analysis, similarly to OLI, MSI images were resampled systematically in 30 m by 30 m pixel size considering UTM projection and WGS84 datum. The comparisons of the surface reflectance, and derived SSSI and SEPM were undertaken in the same way for simulated and images data using regression analysis, coefficient of determination ($R^2$), and *Root Mean Square Difference* (RMSD). The results obtained demonstrate that the statistical fits between SMI and OLI simulated surface reflectance over a wide range of soil samples with different salinity degrees reveals an excellent linear relationship ($R^2$ of 0.99) for all bands, as well as for SSSI and SEPM. The RMSD values are null between the NIR and SWIR homologous bands, and are insignificant for the other bands (i.e., 0.003 for coastal and 0.001 for the blue, green, and red bands). Moreover, the SSSI show an RMSD of 0.0007 and the SEPM express an excellent RMSD around 0.5 $dS.m^{-1}$ (electrical conductivity unit) reflecting a relative error that varies between 0.001 and 0.05 for salinity classes varying between 2.5 $dS.m^{-1}$ (non-saline) and 600 $dS.m^{-1}$ (extreme salinity), respectively. Likewise, the two used pairs of images exhibited very significant fits: $R^2$ of 0.93 for the costal and $R^2 \geq 0.96$ for the other bands of land surface reflectance, and $R^2$ of 0.95 for SSSI and SEPM. Excellent consistency was also observed between the derived products of the two sensors, yielding a RMSD values less than 0.029 (reflectance units) for the bands and less than 0.004 for SSSI. While, the calculated RMSD for the SEPM fluctuate between 0.12 and 2.65 $dS.m^{-1}$, respectively, of non-saline and extreme salinity classes, which means that the relative errors varies between 0.005 and 0.03 for the considered soil salinity classes. Therefore, in the light of these results obtained, we can conclude that the MSI and OLI sensors can be used jointly to characterize and to monitor accurately the soil salinity and it's dynamic in time and space in arid landscape, provided that rigorous preprocessing issues (sensor calibration, atmospheric corrections, and BRDF normalization) must be addressed before.**

***Index Terms* -** Sentinel-MSI, Landsat-OLI, Spectroradiometric measurements, Simulated data, Images data, Soil salinity, Soil salinity and sodicity index, Semi-empirical model, Arid landscape

## I. INTRODUCTION

ARID landscapes are seriously facing challenge of spatial and temporal distribution of soil salinity, particularly during drought periods [1], due to water quality and scarcity, the high temperature and the increased

A. Bannari directs the company Space Pix-Map International Inc., # 31 De-la-Clairière Street J8R-3R7, Gatineau (Québec) Canada.
Tel.: +1-819-230-7186; Email: abannari@agu.edu.bh and abannari@bell.net
N. Hameid with the Department of Geoinformatics, College of Graduate Studies, Arabian Gulf University, Manama 26671, Kingdom of Bahrain.
A. Abuelgasim with the Department of Geography and Urban Sustainability, United Arab Emirates University, Al-Ain, Abu Dhabi 15551, United Arab Emirates.
A. El-Battay with the International Center for Biosaline Agriculture (ICBA), Dubai, United Arab Emirates.

evapotranspiration rate [2]. In addition to water stress, these landscapes are vulnerable to salinization, marginality and desertification as a consequences of human activities [3] and global climate change impact [4]. Obviously, these factors have significant impacts on land degradation, crop production, food security, economic aspects and infrastructure; as well as ecosystem functionality, human wellbeing and sustainable development [5]. Around the world, soil salinity affect approximately 40 to 45% of the Earth land, especially in semi-arid and arid landscapes [6], and the global cost of irrigation-induced salinity is estimated around 11 billion US$ a year [7]. To remedy this situation in vulnerable landscape to salinization, there are methods available to slow down the processes and, sometimes, even reverse them. However, remedial actions require reliable information to help set priorities and to choose the type of action that is most appropriate for a specific location. In affected areas, farmers, soil managers, scientists, and agricultural engineers need accurate and reliable information on the nature, extent, magnitude, severity, and spatial distribution of the salinity against which they could take appropriate measures [8].

Soil salinity monitoring in space and time is complicated by salinity's dynamic nature, due to the influence of management practices, water table depth, soil permeability, micro-topography, water use, rainfall, and salinity of groundwater. When the need for repeated measurements in time is multiplied by the extensive requirements of a single sampling period, the expenditures of time and effort with conventional soil sampling procedures increase proportionately. In general, measuring electrical conductivity extracted from a saturated soil paste at the laboratory ($EC_{-Lab}$) is the most accurate method used for soil salinity mapping [9]. Unfortunately, this method is expensive and time consuming, especially for regular monitoring over a long period, and for comparisons over large areas [10,11]. During the last two decades, remote sensing technology and image processing methods have outperformed these conventional methods. Currently, new remote sensing satellite instruments measuring soil salinity, coupled with modeling, programming, and mapping in GIS environment have significantly improved the potential for soil salinity monitoring in space with a very high temporal frequency [12-16]. The main advantage of remote sensing is the ability to map large areas at a relatively low cost by collecting information at regular intervals; therefore, monitoring becomes easier. This allows not only for the appropriate remedial action to be taken, but also for the monitoring of the effectiveness of any ongoing remediation or preventative measures, which facilitate monitoring, management and decision-making [17].

Furthermore, actually, the availability of the new generation of medium spatial resolution, such as Multi-Spectral Instruments (MSI) on board Sentinel-2 satellites and Operational Land Imager (OLI) sensor installed on Landsat-8 platform, offers new opportunities for long-term high-temporal frequency for Earth surfaces' observation and monitoring [18]. The free-availability of their data significantly advances the virtual constellation paradigm for mid-resolutions land imaging [19-21]. Thanks to the improvement of their spectral, radiometric, and temporal resolutions, they can expand the range of their applications to several natural resources and environmental domains for monitoring, assessing and investigating [22]. The orbits of the both satellites are designed to ensure a revisiting interval time of approximately less than 5 days [23], thereby substantially increasing monitoring capabilities of the Earth's surface and ecosystems [24]. Their spectral resolutions and configurations are designed in such a way that there is a significant match between the homologous spectral bands [24,25]. However, depending on the spectral sensitivity of the target under investigation [26], sensor radiometric drift calibration [27], atmospheric corrections [28], surface reflectance anisotropy [29], and sensors co-registration [30,31], it is plausible that the natural surface-reflectance between MSI and OLI may be different. In addition, the relative spectral response profiles characterizing the filters (spectral responsivities) of the both instruments are not identical between the homologous bands, so some differences are probably expected in the recorded land-surface reflectance values; therefore, their data cannot be reliably used together [32,33]. Obviously, the importance of these differences depends on the application (spectral characteristics of the observed target) and on the approach adopted to perform time series analyses, mapping or change detection exploiting both instruments [26]. For instance, it is plausible that the extraction of soil salinity information in time over arid landscape using surface reflectance, empirical, semi-empirical, and/or physical approaches, can affected the results comparison.

Likewise, in addition to the remote sensing sensors technology improvement and innovation, several image processing methods and models were developed and applied for soil salinity retrieval. Based on simulated data and satellite images acquired with several sensors (TM, ETM+, OLI, MSI, ALI EO-1, and WorldView-3), numerous studies revealed that spectral confusion occurs in the visible and near-infrared (VNIR) spectral domain between the salt crust and the artifacts of soil optical properties. While other studies have shown that the shortwave infrared (SWIR) spectral bands allows better discrimination among salt-affected soil classes. Shrestha [34] concluded that the SWIR bands were the most correlated with soil salinity. Bannari *et al.* [14, 35-37] found that the SWIR bands of ALI, OLI, SMI and WV3 offers the best potential for soil salinity detection and discrimination. Considering different soil types and geographic locations, Leone *et al.* [38], Odeh and Onus [39], and Zhang *et al.* [40] demonstrated that the SWIR bands could be used for soil salinity estimation in agricultural fields better than other spectral domains. Chapman *et al.* [41] showed that the SWIR bands of TM provide excellent discrimination of evaporite mineral zones in salt flats. Drake [42] described the various absorption peaks of the salts found in evaporite minerals in the SWIR wavelengths. The study undertaken by Hawari [43] showed that the absorption features in SWIR bands are consistent with the detection of the gypsum, halite, calcium carbonate, and sodium bicarbonate. According to Nawar *et al.* [44], the SWIR bands of ASTER exhibited the highest contribution for soil salinity estimation. Moreover, another study [45] indicated that the SWIR bands of the ETM+ sensor increases the accuracy of the soil salinity prediction.

This paper analyse and compare the difference between land-surface reflectance in the homologous spectral bands of MSI and OLI sensors, VNIR and SWIR, for soil salinity dynamic monitoring in an arid landscapes. In addition, comparisons were

This article has been accepted for publication in a future issue of this journal, but has not been fully edited. Content may change prior to final publication. Citation information: DOI 10.1109/JSTARS.2020.2995543, IEEE Journal of Selected Topics in Applied Earth Observations and Remote Sensing

carried out in terms of conversion of these surface reflectance to the *Soil Salinity and Sodicity Index* (SSSI) and to the *Semi-Empirical Predictive Model* (SEPM) for salt-affected soil mapping.

## II. MATERIAL AND METHOD

Fig. 1 illustrate the used methodology; which is structured in four steps exploiting two independent datasets: simulated and images data. For simulated data, a field campaign was organized and 160 soil samples were collected with various degrees of soil salinity classes (i.e., extreme, very high, high, moderate, and low) including non-saline soil samples. The bidirectional reflectance factor was measured above each soil sample in a Goniometric-Laboratory using an *Analytical Spectral Devices* (ASD) FieldSpec-4 high resolution (Hi-Res) spectroradiometer [46]. The required preprocessing steps to allow their meaningful and accurate use and comparison were then carried out. Indeed, all measured spectra were resampled and convolved in the solar-reflective spectral bands of Sentinel-MSI and Landsat-OLI sensors using the *Canadian Modified Simulation of a Satellite Signal in the Solar Spectrum* (CAM5S) [47] based on Herman radiative transfer code (RTC), and the relative spectral response profiles characterizing the filters of each instruments in the VNIR and SWIR bands. While, the two pairs of images were acquired with Sentinel-MSI and Landsat-OLI sensors over the same study site in July 2015 and August 2017 with one day difference between each pair. They were not cloudy, or cirrus contaminated, and without shadow effects because topographic variations are absent in the study area. They were radiometrically and atmospherically corrected to transform them to the ground surface reflectance, and the *Bidirectional Reflectance Distribution Function* (BRDF) were normalized to allow their meaningful comparison correctly. Finally, the standardized reflectance (simulated and images data) were converted in terms of SSSI and SEPM for soil salinity mapping. For comparison and sensor differences quantification, statistical fits were conducted using linear regression analysis ($p < 0.05$), coefficient of determination ($R^2$), and the *Root Mean Square Difference* (RMSD) was calculated. It is important to precise that subsequently to the spectroradiometric measurements, in the laboratory, soil chemical analyses (cations and anions: $Ca^{2+}$, $Mg^{2+}$, $Na^+$, $K^+$, $Cl^-$ and $SO_4^{2-}$), the soil reaction (pH) and the electrical conductivity ($EC_{Lab}$) were extracted from a saturated soil paste, as well as the sodium adsorption ratio (SAR) being calculated [9]. These parameters provides reliable information about the degree of salinity in each considered soil sample, and thus help to understand the close relationship between the salt content values in each soil sample and its spectral behavior.

Fig 1. Flowchart of the methodology.

### *A. Study Site*

The Kingdom of Bahrain (25°32′ and 26°00′N, 50°20′ and 50°50′E) is an archipelago of 33 islands located in the Arabian Gulf, east of Saudi Arabia and west of Qatar (Fig. 2) with a total land area of about 778.40 km$^2$. According to the aridity criteria and the great variations in climatic conditions, Bahrain has an arid to extremely arid environment [48]. The climate is characterized by very high summer temperatures of an average 45°C during June-September and an average of approximately 17°C in winter from December-March. Rain is sparse, and occurs primarily from November to March, with an annual average of 72 mm, sufficient only to support the most drought-resistant desert vegetation. Mean annual relative humidity is over 70% due to the surrounding Arabian Gulf water, and the annual average potential evapotranspiration rate is 2099 mm [49]. Under such climatic conditions, where precipitation is excessively low to maintain a regular percolation of rainwater through the soil, soluble salts are accumulated in the soil, influencing soil properties and environment causing low soil productivity. Indeed, these factors have significant impacts on land degradation, crop production, economic aspects, and infrastructure, as well as ecosystem functionality, human wellbeing, and sustainable development [50]. Geologically, Bahrain is characterized by Eocene and Neocene rocks, which are partly covered by Quaternary sediments and a complex of Pleistocene deposits. The dominant rocks are limestone and dolomitic-limestone with subsidiary marls and shales. The leading structure is the north–south axis of the main dome, with minor cross-folds predominantly tilting from northeast to southwest. The beds are gently inclined towards the coast from the center of the main island. The fringes of Bahrain are covered by more recent marine and Aeolian sand dunes, which were derived from the Arabian land connection across the present Arabian Gulf.

Fig 2. Study site (Kingdom of Bahrain).

### *B. Soil sampling and laboratory analyses*

The soils of Bahrain are characterized by five different classes associated with moderate to shallow depths and are closely related to the terrain geology and geomorphology [51]. The natural Solonchak describes soils with no agricultural activities and retain a significant gypsum content (high and very high salinity). Then, there is the cultivated Solonchak soil class, which is located in areas either currently or previously exposed to agricultural activities. The Regosols soil class with moderate salinity is depicted as a mixture of raw minerals as well as the natural Solonchak soils, with the possibility for growing scattered halophytic plants. The miscellaneous land class that is represented by a composition of silts and fine sands with low salinity is suitable for agriculture. Finally, there is the non-saline soil class, which is imported to build artificial islands.

Based on Bahrain salt-affected soil map, six salinity classes are considered (Fig. 3): extreme (class 1), very high (class 2), high (class 3), moderate (class 4), low (class 5) and non-saline (class 6). The extreme soil salinity class is characterized by the presence of high contents of soluble salts and the surface salt crust, which is sabkha (C1 in Fig. 3). They are natural solonchaks soil (loamy and sandy, highly gypsiferous) devoid of any vegetation. The very high saline soils (class 2) are often encrusted with an efflorescence of salt crystals and a well-developed platy structure, which looks like the creation of a new sabkha (C2 in Fig. 3). The high salinity soils (class 3) are composed of fine, white, sand-sized shell gravel and gravelly sand (C3 in Fig. 3); the surface layers are sometimes cemented

This article has been accepted for publication in a future issue of this journal, but has not been fully edited. Content may change prior to final publication. Citation information: DOI 10.1109/JSTARS.2020.2995543, IEEE Journal of Selected Topics in Applied Earth Observations and Remote Sensing

by salt and are completely devoid of vegetation. The moderate soil salinity (class 4) is the dominant class in the southern half of Bahrain Island (C4 in Fig. 3). It is calcareous to highly calcareous, with calcium carbonate and dominated by shells and sand. Very sparse and scattered clumps of halophytic (salt tolerant) plants are observed in this class area. Furthermore, in the northwest part of Bahrain Island we find the spatial distribution of low salinity soils (class 5), whit acceptable fertility potential. This class is the only cultivated area in Bahrain (about 8% of the total area of the country), which is equipped with micro drip irrigation systems (C5 in Fig. 3). Finally, the non-saline soil (class 6) describes accurately the man-made (artificial) infrastructure, industrial and urban zones (C6 in Fig. 3).

Fig 3. Photos of the six considered soil salinity classes (C1 to C6).

A total of 160 samples were collected during a very dry period from 2 to 7 April 2016, based on the spatial representativeness of the six major soil classes as discussed above. Samples were collected from the dry upper layer from 0 to 5 cm deep (crust) considering an area about 50 × 50 cm without vegetation residue (senescent or green) and moisture-free (Fig. 3). Under the field conditions the soil moisture contents remained very low and not exceeded 0.08% in the all considered samples (Loamy-sandy, silty-sandy, silty-clay-loam, highly gypsiferous), thus minimizing the impact of soil moisture on the measured spectra (Fig. 4) [52,53]. Moreover, observations and remarks about each sample (color, brightness, texture, etc.) were noted. The location of each point was automatically labeled and recorded using a 35-mm digital-camera equipped with a 28-mm lens and accurate GPS survey ($\sigma \leq \pm 30$ cm) connected in real-time to the GIS database.

After spectroradiometric measurements, which are described below, soil samples were crushed and then sieved to obtain the < 2mm fraction. Then, standard USDA laboratory methods and procedures [9] were used to measure the pH, the electrical conductivity (EC-$_{\text{Lab}}$), and the major soluble cations (Na$^{+}$, K$^{+}$, Ca$^{2+}$+, and Mg$^{2+}$) and anions (CO$_3^{2-}$, HCO$_3^{-}$, Cl$^{-}$, and SO$_4^{2-}$) using extraction from a saturated soil paste, and the SAR was also calculated [54]. In addition to the field observations, these parameters are considered in this study for the only purpose to provide reliable information about the degree of salinity content in each considered soil sample assisting the interpretation of spectroradiometric measurements and selected pixels from the used images.

Fig 4. Spectral signatures of 160 soil samples with different degrees of salinity.

### *C. Spectroradiometric Measurements*

Spectroradiometric measurements were acquired in the Goniometric-Laboratory. The bidirectional reflectance spectra of soil samples were measured in air-dried conditions using an ASD (Analytical Spectral Devices Inc., Longmont, CO, USA) FieldSpec-4 Hi-Res (high resolution) spectroradiometer [46]. This instrument is equipped with two detectors operating in the VNIR and SWIR, between 350 and 2500 nm. It acquires a continuous spectrum with a 1.4 nm sampling interval from 350 to 1000 nm and a 2 nm interval from 1000 to 2500 nm. The ASD resamples the measurements in 1-nm intervals, which allows the acquisition of 2151 contiguous bands per spectrum. The sensor is characterized by the programming capacity of the integration time, which allows an increase of the signal-to-noise ratio (SNR), as well as stability. The data were acquired at nadir with a FOV of 25° and a solar zenith angle of approximately 5° by averaging 40 measurements. The ASD was installed at a height of 60 cm approximately over the target, which makes it possible to observe a surface of approximately 700 cm$^2$. A laser beam was used to coincide the center of the ASD-FOV with the center of the target under measurements. The reflectance factor of each soil sample (Fig. 4) was calculated by rationing target radiance to the radiance obtained from a calibrated “spectralon panel” in accordance with the method described in Jackson *et al.* [55]. Corrections were made for the wavelength dependence and non-Lambertian behavior of the panel [56,57].

### *D. Sentinel-MSI and Landsat-OLI simulated data*

The measured bidirectional reflectance factors using the ASD have a 1-nm interval, which allows the acquisition of 2151 contiguous hyperspectral bands per spectrum. However, most multispectral remote sensing sensors measured the reflectance that is integrated over broad bands. Consequently, the measured spectra of each soil sample was resampled and convolved to match the MSI and OLI solar-reflective spectral responses functions characteristics (Fig. 5). In this step, the resampling procedure considers the nominal width of each spectral band (Table I). Then, the convolution process was executed using the CAM5S RTC [47 ]. This fundamental step simulates the signal received by the MSI and OLI sensors at the top of the atmosphere from a surface reflecting solar and sky irradiance at sea level considering the filters responsivities of individual sensor band (Fig. 5), and assuming ideal atmospheric conditions without scattering and without absorption [58-61]. To understand correctly gain insights into any reflectance differences between the two sensors due only to their spectral responses functions differences, the 160 simulated sensor reflectance values were generated with various salinity degrees. These simulated reflectance in the VNIR and SWIR spectral band were fitted between MSI and OLI homologous bands using regression analysis ($p < 0.05$). This statistical examination step was used to evaluate the strength of the relationship between the reflectance information in homologous spectral bands, and the possibility to involve the both sensors together for salt-affected soil monitoring in time. It is important to note that the MSI-NIR-2 broad band (band-8: 785 - 900 nm) is not considered in this study because it is not a real homologous band of OLI-NIR, and it has a greatest reflective band difference with the OLI-NIR (851–879 nm). In fact, the OLI-NIR spectral response function intersects with only 20% of the MSI-NIR-2 response function. Moreover, the MSI red-edge bands were not considered also as they are not acquired by the OLI sensor.

This article has been accepted for publication in a future issue of this journal, but has not been fully edited. Content may change prior to final publication. Citation information: DOI 10.1109/JSTARS.2020.2995543, IEEE Journal of Selected Topics in Applied Earth Observations and Remote Sensing

Fig 5. Sentinel-MSI and Landsat-OLI relative spectral response profiles characterizing the filters of each spectral band in the VNIR (a), and the SWIR (b).

### *E. Sentinel-MSI and Landsat-OLI images data*

The Sentinel-2 “A and B” satellites were launched, respectively, on June 23rd 2015 and March 7th 2017 with the identical MSI sensors on board. They were proposed to provide continuity to the SPOT missions [24] and to improve the Landsat-OLI temporal frequency. In fact, the synergy between Sentinel-MSI (A and B) and Landsat-OLI significantly increase the temporal resolution for several environmental and natural resource applications, such as the vigor of vegetation cover, emergency management, soil salinity dynamics, water quality, and climate change impact analysis at local, regional, and global scales. Sentinel-MSI is the result of close collaboration between the European Space Agency, the European Commission, industry, service providers, and data users. The MSI images the Earth’s surface reflectivity with a large FOV (20.6º) in 13 spectral bands, four bands with 10-m pixel size (blue, green, red and NIR-1), six bands with 20-m (Red-Edge, NIR-2 and SWIR), and three bands with 60-m bands (coastal, water vapor and cirrus). The swath of each scene is 290 km, permitting global coverage of the Earth’s surface every 10 days. The MSI radiometric performance is coded in 12 bits, enabling the image acquisition in 4095 digital numbers, ensuring radiometric accuracy of less than 3% and an excellent SNR [27, 62]. The geometric registration precision is better than 0.15 pixels, and it was shown that no visual obvious mis-registration was observed when the multi-temporal MSI data were used [31]). Table I summarizes the effective bandwidth characteristics for MSI.

TABLE I. The Sentinel-MSI and Landsat-OLI effective bandwidths and characteristics ($\lambda$ = wavelength, SNR = signal to noise ratio).

Furthermore, since 1972, the Landsat scientific collaboration program between the NASA and USGS constitute the continuous record of the Earth’s surface reflectivity from space. Indeed, the Landsat satellites series support nearly five decades of a global moderate resolution data collection, distribution and archive of the Earth’s continental surfaces [63,64] to support research, applications, and climate change impact analysis at the global, the regional and the local scales [19, 65,66]. In February 11th, 2013, the polar-orbiting Landsat-8 satellite was launched, transporting two push-broom instruments: OLI and TIRS. The OLI sensor collects land-surface reflectivity in the VNIR, SWIR, and panchromatic wavelength with a FOV of 15° covering a swath of 185 km with 16 days’ time repetition at the equator. The band passes are narrower in order to minimize atmospheric absorption features [67], especially the NIR spectral band (0.865 μm). Two new spectral bands have been added: a deep blue visible shorter wavelength (band 1: 0.433 - 0.453 μm) designed specifically for water resources and coastal zone investigation, and a new SWIR band (9: 1.360 - 1.390 μm) for the detection of cirrus clouds. Moreover, the OLI design results in a more sensitive instrument with a significant amelioration of the SNR radiometric performance quantized over a 12-bit dynamic range (Level 1 data), raw data are delivered in 16 bit. This SNR performance and improved radiometric resolution provide a superior dynamic range and reduce saturation problems associated with globally maximizing the range of land-surface spectral radiance and, consequently, enable better characterization of land-cover conditions [68 45]. According to Gascon *et al.* [69 46] and Markham *et al.* [27], Landsat-OLI and Sentinel-MSI on orbit reflective wavelength calibration is better than 3%. From geometric point of view, Stumpf *et al.* [70 47] obtained a co-registration accuracy between images provided by both missions around ± 3 m by reference to accurate ground control point’s measurements. Table I summarizes the effective bandwidth characteristics for OLI. In this research, two pairs of images data were used. They were acquired during the the hottest period in the Middle-East with temperatures around 46-48°C. They were not cloudy and not contaminated with cirrus, without significant topographic variations and, consequently, the shadow effects were absent in the study area. The first pair were acquired with one day difference, the 29th and 30th of July 2015 for OLI and MSI, respectively. The second pair were also recorded with one day difference in 18th and 19th August 2017, respectively, for MSI and OLI (Fig. 6). This very short time between each pair (MSI and OLI) data acquisition is so important to minimize the impact of land-use and soil surface conditions changes between these sensor observations.

Fig 6. True color composite of raw OLI and MSI images data acquired over Kingdom of Bahrain in July 2015 (left) and August 2017 (right).

### *F. Images data preprocessing*

Prior to launch, the sensors are subject to rigorous radiometric and spectral characterization and calibration. However, post-launch absolute calibration is an important step to establish the relationship between at-sensor radiance and the digital number output for each pixel in the different spectral bands. Sensor radiometric calibration and atmospheric corrections (scattering and absorption) are fundamental preprocessing operations to restore the images radiometric quality at the ground level. The changes caused by these artifacts can be mistakenly attributed to changes in the land use and ground bio-physiological components, and errors can propagate in all subsequent image processing steps, such as spectral indices calculations, multi-temporal analysis, climate change modeling, etc. [71,72]. For converting the measured digital numbers by MSI and OLI sensors to the apparent radiance, the values of the solar zenith angle and rescaling coefficients (gain and offset) delivered by USGS-EROS and ESA centers were used. Moreover, the CAM5S RTC [47] was used for atmospheric conditions simulation to calculate all the requested atmospheric correction parameters for MSI and OLI spectral bands. This RTC simulates the signal measured at the TOA from the Earth’s surface reflecting solar and sky irradiance at sea level, while considering the sensors characteristics, such as the band passes of the solar-reflective spectral bands (Fig. 5), satellite altitude, atmospheric condition, atmospheric model, Sun and sensor geometry, and terrain elevation. Consequently, all the requested atmospheric correction parameters were calculated and applied to transform the apparent reflectance at the TOA to the ground reflectance. Table II summarizes the input parameters for the CAM5S RTC for each pair of images. To preserve the radiometric integrity of the images, absolute radiometric calibration and atmospheric effects corrections were combined and corrected in one step [73] to generate ground surface reflectance images using the Canadian image processing system PCI-Geomatica.

Furthermore, knowing that Earth's natural surfaces do not have a Lambertian spectral behavior, because both solar and observing zenith angles exert a radiometric distortion impact on surfaces reflectance, the BRDF problem was normalized. According to Roy *et al.* [66] along the Landsat-OLI bands (edges by reference to the image center) the reflectance can vary by less than 6% due to this BRDF effects. Moreover, Roy *et al.* [29] reported that this problem can affect the Sentinel-MSI bands by approximately 8% because of its large FOV. Certainly, these differences may constitute a source of errors for biophysical and physiological parameters extraction, as well as for general remote sensing applications because their values as mentioned before are relatively more meaningful than the sensor calibration errors [27] and atmospheric corrections [69]. To normalize the BRDF influence on the ground surface reflectance images of MSI and OLI, a semi-empirical approach [74] was applied in this research.

TABLE II. Input parameters for the CAM5S RTC (ASL: above sea level; GMT: Greenwich Mean Time; ppm: parts per million).

### G. Data conversion

For soil salinity detection and mapping, many soil salinity spectral indices and models have been proposed in the literature [75-78]. A comparative study among several semi-empirical predictive models based on salinity indices, such as *Brightness Index* (BI), *Normalized Difference Salinity Index* (NDSI), *Salinity Indices* (SI), *ASTER Salinity Index* (SI-ASTER), *Soil Salinity and Sodicity Index* (SSSI), etc. was achieved for accurate salt-affected detection in irrigated agricultural land (slight and moderate salinity classes) in North Africa and in the arid landscape (slight, moderate, strong and very strong salinity classes) in Middle-East [36, 79,80]. The results of these studies showed that the SEPM model based on SSSI, which integrate the SWIR bands, provided the best accuracy for salt-affected soil classes' detection and mapping. Consequently, in this study, the comparisons of SSSI and SEPM are undertaken in the same way as surface reflectance derived from simulated and images data to quantify the impact differences between relative spectral response profiles characterizing the filters of homologous bands of MSI and OLI sensors. The SSSI and SEPM equations are as follow [35,36]:

$$EC_{-\text{Predicted}} = C^{ste} \,.\, [\ 4521.\,(SSSI)^2 + 125.\,(SSSI) + 0.41\ ] \quad (1)$$

$$SSSI = (\rho_{SWIR\text{-}1} \cdot \rho_{SWIR\text{-}2} - \rho_{SWIR\text{-}2} \cdot \rho_{SWIR\text{-}2}) / (\rho_{SWIR\text{-}1}) \quad (2)$$

Where:

$EC_{-\text{Predicted}}$: SEPM,

$\rho_{SWIR\text{-}1}$: Reflectance in MSI and OLI SWIR-1 channel, and

$\rho_{SWIR\text{-}2}$: Reflectance in MSI and OLI SWIR-2 channel.

$C^{st}$: Scaling factor, which theoretically enables an up-scaling between the spatial information measured in the field and its homologous information derived from the image [81]. However, in this study case its value is equal to one because we are comparing data from the same sources (MSI to OLI simulated data, or image to image), and not from the field to the image.

### H. Statistical analyses

As discussed previously, the MSI and OLI relative spectral response profiles characterizing the filters of each spectral band are relatively different (Fig. 5). To examine the impact of this difference, statistical analyses were computed using "Statistica" software considering simulated and images data. The relationships between derived product values (reflectance, SSSI and SEPM) from MSI against those from OLI were analyzed using a linear regression model ($p < 0.05$). As well, the $R^2$ was used to evaluate the strength of this linear relationship. For this process, the resampled and convolved spectra of 160 soil samples and images ground reflectance data were used, and the homologous values in VNIR and SWIR bands of MSI and OLI were compared using the 1:1 line. Ideally, these independent variable values should have a correspondence of 1:1. Additionally, the RMSD between the both sensors was derived for simulated and images data as follow [21, 82]:

$$RMSD = \sqrt{\frac{\sum_i^n (v_i^{OLI} - v_i^{MSI})^2}{n}} \quad (3)$$

where RMSD is the root mean square difference between corresponding Landsat-OLI and Sentinel-MSI variables values (reflectance, SSSI, and SEPM) derived from simulated spectra and images-pixels, $v_i$ is the variable under analysis and " i " is the number of variable (i = 1 to n).

## III. RESULTS ANALYSES

### A. Soil laboratory analysis and simulated data comparison

Fig. 4 show that overall, the spectral signatures of the 160 considered soil samples are controlled by the type of salt existing in each soil sample, such as sulfates, chlorides, and/or carbonates. The results showed different amplitudes and several absorption features depending on the chemical compositions and the mineralogy of the existing salts in the selected soil samples. Moreover, the spectral signatures are also influenced by several factors, such as mineralogical composition, impurity, structure, and texture of the soil and salt crystals, and the soil optical properties (color brightness, and roughness), particularly in the VNIR spectral domain [14]. Furthermore, the laboratory analyses of all soil samples revealed that the moisture content values are distributed in a very limited range between 0 and 0.08%, thus minimizing the impact of moisture content on the measured spectra (Fig. 4). In fact, only three weak absorption bands near 1350, 1800, and 2208 nm were observed in some samples (atmospheric water vapor absorption features at 1440 and 1920 nm are note considered in this analysis). While, the other absorption features are automatically linked to the salt mineralogy, particularly the gypsum, sodium, chloride, halite, calcium carbonate, and sodium bicarbonate, which reveals significant absorption features at 980, 1000, 1190, 1210, 1400, 1450, 1490, 1540, 1748, 1780, 1800, 1900,1945, 1975, 2175, 2215, 2265, and 2496 nm [14]. These observations corroborate findings of other studies [14,43, 53].

Otherwise, the major exchangeable cations and anions in the considered six soil sample classes ($Ca^{2+}$, $Mg^{2+}$, $Na^{+}$, $K^{+}$, $Cl^{-}$ and $SO_4^{2-}$), pH, EC-$_{Lab}$, and SAR values were calculated from the sampling points representing each soil class separately and summarized in the Table III. The laboratory analyses revealed a very high concentration of sodium ($Na^{+}$) and dominant chloride anion ($Cl^{-}$). Globally, the values of EC-$_{Lab}$, $Na^{+}$, and SAR increase gradually and very significantly from non-saline soil to extreme soil salinity (sabkha). Indeed, the non-saline and low soil salinity classes, which support the agricultural system in Bahrain, are characterized by low EC-$_{Lab}$ ($2.6 \leq$ EC-$_{Lab} \leq 4.4$ dS.m$^{-1}$) and SAR ($\leq 10.3$). The moderate salinity class was characterized by EC-$_{Lab}$ around 7.4 dS.m$^{-1}$, and SAR nearby 12.7 representing the dominant soil class in Bahrain and is a part of the Regosols soil category that allows for the growth of halophytic plants. Contrariwise, the other three soil salinity classes with high, very high and extreme salinity content showed exceptional EC ($67 \leq$ EC-$_{Lab} \leq 600$ dS.m$^{-1}$) and very high SAR ($\geq 99.2$) values. These three classes represent the natural Solonchak soil category. While, the pH values (7.1 to 8.6) are very informative as regards the preponderance of carbonate and the presence of bicarbonate in the soils which contribute significantly to the alkalinity aspect of the soil. Clearly, these results confirm our choice of different soil salinity classes that represent the truth of arid landscapes, which is fundamental for the analyses of the impact of the spectral response functions difference on the surface reflectance and the products derived from the homologous spectral bands (VNIR and SWIR) of the MSI and OLI sensors.

TABLE III. Laboratory determination of pH, EC-$_{Lab}$ and ions content in the different soil salinity classes.

Fig. 7 illustrate the scatter plots of SMI and OLI simulated surface reflectance values at the top of the atmosphere, which were generated from 160 soil samples with unlike salinity degrees ($2.6 \leq$ EC-$_{Lab} \leq 600$ dS.m$^{-1}$) to analyze the impact of differences in reflectance due exclusively to dissimilarities in spectral response function between homologous spectral bands. These scatter plots reveals a very good linear relationship ($R^2$ of 0.999) between homologous bands whit the slopes and intercepts very near to unite and zero, respectively. Table IV summarizes the obtained regression fit equations, the coefficient of determination and the RMSD between MSI and OLI simulated surface reflectance in the homologous bands, as well as the derived SSSI and SEPM products. The RMSD values are null between the NIR and SWIR homologous bands, and are insignificant for the other bands (i.e., 0.003 for coastal and 0.001 for the blue, green, and red bands). Highlighting the good behavior of SWIR bands, the calculated SSSI values fit perfectly with the line 1:1 ($R^2$ of 0.9996) showing a slope of 1.01, intercept of 0.002, and RMSD of 0.0007 (Fig. 8). Moreover, independently to the degrees of salinity in the considered soil samples, the simulated SEPM values fit perfectly with 1:1 line expressing an excellent coefficient of determination ($R^2$ of 0.9994) and a slope near to the unit (0.995). The calculated RMSD for the SEPM vary between 0.003 and 0.5 dS.m$^{-1}$ (electrical conductivity unit) reflecting a relative error that varies between 0.001 and 0.05 for salinity classes varying between 2.5 (non-saline) and 600 dS.m$^{-1}$ (extreme salinity). Moreover, this difference is identical to the electrical conductivity accuracy measurement in the filed using electronical instruments [83]. These results pointed out that MSI and OLI sensors can be combined for high temporal frequency to monitor soil salinity dynamic in time and space in an arid landscape. However, it is important to remember that these simulations took place in a Goniometric-Laboratory using close range measurements protocol assuming indirectly that the measured surfaces are homogeneous with Lambertian reflectance (by reference to spectralan). In addition, the atmospheric scattering and absorption are absent, errors related to radiometric calibration and geometric location are also absent, no topographic variation, no residual clouds or shadows, and no BRDF impact. Evidently, these simulations in a controlled environment are ideal comparatively to the real Earth observation conditions using images data acquired with MSI and OLI sensors and covering a large pixel surface (900 m$^2$) with mixt information.

Fig 7. Compared surface reflectance simulated and convolved in Sentinel-MSI and Landsat-OLI homologous spectral bands.

Fig 8. Compared SSSI (left) and SEPM (right) derived from Sentinel-MSI and Landsat-OLI simulated data.

TABLE IV. Regression fit equations between MSI and OLI simulated surface reflectance in the homologous spectral bands, and the derived SSSI and SEPM

### *B. Images results analysis*

The spectral bands of MSI have unlike spatial resolutions (10, 20 and 60-m) than those of OLI bands (30-m). To handle this spatial difference and to generate data correspondingly to OLI images for analyses, MSI images were resampled automatically in 30-m pixel size considering UTM projection and WGS84 datum. Based on the measured GPS ($\sigma \leq 30$ cm) coordinates location, the considered 160 sampling points representing all salinity classes (approximately 26 pixels per class) were carefully located and selected from the homologous spectral bands in the booth pair of images. Then, comparisons of the surface reflectance, and derived SSSI and SEPM were undertaken in the same way as for the simulated data using regression analysis, $R^2$, and RMSD. Since the results obtained from the two pairs of images are similar (Table V), only the results retrieved from the pair acquired in August 2017 are presented in Fig. 9. This scatter plots shows the relationship between surface reflectance in the VNIR and SWIR homologous bands of SMI and OLI sensors acquired over a wide range of soil samples with different salinity degrees ($2.6 \leq$ EC-$_{Lab} \leq 600$ dS.m$^{-1}$). A very good linear relationships between all homologous bands are observed with the slopes and intercepts near to unite and zero, respectively. The used images in each pair had very significant fits ($R^2 \geq 0.96$) for green, red, NIR and SWIR homologous spectral bands (Fig. 9 and Table V). For these bands, the majority of sampling points are located around the line 1:1. While, the coastal and blue bands fits with $R^2$ of 0.93 and 0.96, respectively. Although these last two bands depicts a good fit to the 1:1 line, in general the reflectance are relatively over-estimated in MSI than in OLI. This is likely due to the correction of scattering effects by aerosols in these short wavelengths, as well as to the OLI medium spatial resolution compared to the original pixel size of MSI. These observations has been also noted in other studies [21]. Furthermore, the RMSD values are insignificant for the NIR and SWIR homologous bands ($\leq 0.009$), and are very small ($\leq 0.029$) in the visible bands (Table V). Globally, the reflectance in OLI visible bands are slightly lower against those in MSI.

Fig. 10 illustrate the relationship between the derived SSSI and SEPM products from MSI and OLI data acquired in 2017. The SSSI values fit significantly with the line 1:1 ($R^2$ of 0.95) showing a slope of 0.97, intercept of 0.00, and RMSD of 0.004. Moreover, the predicted salinity values using the SEPM are fitting well with 1:1 line expressing an excellent coefficient of determination ($R^2$ of 0.95) between the derived information from the two sensors, with a slope of 0.97 (near to the unit) and intercept of 1.46. This scatter-plot showed also a relative underestimation of very high salinity class ($200 \leq EC\text{-}_{Lab} \leq 600$ $dS.m^{-1}$) in the OLI SEPM than that of MSI. Whereas, the RMSD calculated for SEPM varied from 0.12 to 2.65 $dS.m^{-1}$ for non-saline and extreme salinity classes, respectively. Almost similarly to simulated data, these RMSD reflect relative errors varying between 0.005 and 0.03 for the considered soil salinity classes ($2.6 \leq EC\text{-}_{Lab} \leq 600$ $dS.m^{-1}$), which are quite identical to the electrical conductivity accuracy measurements in the filed using electronical instruments [83]. The small RMSD values found between homologous bands of the two considered pair of images (MSI and OLI) and the derived SSSI and SEPM could not be attributed only to sensor spectral response function differences. Definitely, in addition to the unlike spatial resolutions and the resampling MSI pixels, these relative small differences are probably also due to the signal saturation, which resulted by the difference in radiometric resolutions between both sensors. This saturation may be more pronounced over bright and strongly reflective surfaces such as white salt-crust areas, especially when specular effect is strongly pronounced. It can also be magnified by the non-Lambertian surfaces that cause a non-negligible BRDF effects [29], as well as the BRDF standardisation (FOV of ±10.3° for MSI rather than ±7.5° for OLI), which is based on a semi-empirical model [74]. Moreover, it can also be caused by the residual errors of sensor radiometric calibration and atmospheric corrections that are never perfect, particularly at shorter wavelengths where atmospheric scattering impacts are usually greatest, and also because the images have not been atmospherically corrected pixel by pixel but rather band by band.

Fig 9. Compared surface reflectance acquired with Sentinel-MSI and Landsat-OLI spectral bands (VNIR and SWIR) acquired in August 2017.

In general, independently to the used data (simulated or images) the statistical fits found to be highly significant ($0.95 \leq R^2$) and the reached RMSD values ($< 0.029$) where smaller than the accuracy of radiometric calibration process (0.03) as demonstrated by Markham *et al.* [7]. Moreover, despite the small differences especially in coastal and blue bands, these results pointed out that MSI and OLI sensors can be combined for high temporal frequency to monitor soil salinity dynamic in time and space in an arid landscape. However, rigorous preprocessing issues (sensors calibration, atmospheric corrections, and BRDF normalisation) must be addressed before the joint use of acquired data with these two sensors. This results corroborate the finding of Davis *et al.* [84] who have demonstrated that the two sensors have similar salinity modelling skill in Hyde County areas in North Carolina (USA). Moreover, although the present paper is focalising specifically on soil salinity as a specific target, the results obtained are consistent with previous research projects considering several other applications around the world. For instance, comparing surface reflectance and derived biophysical variables over Australian territory, Flood [26] indicated good compatibility between SMI and OLI instruments with RMSD < 0.03 for surface reflectance in VNIR and SWIR bands, and an RMSD around 0.05 for biophysical variables. Pastick *et al.* [85] demonstrated that observations made by MSI and OLI can be used to monitor land-surface phenology accurately in drylands of the Western United States. Vuolo *et al.* [86] compared surface reflectance and biophysical products of many targets over six test sites in Europe showed a good relationship between these two sensors products, yielding RMSD values around 0.03 reflectance units. Some tests performed on simulated data and on real images data acquired simultaneously with MSI and OLI over a wide variety of land cover types (agricultural fields, inland, and open shallow water) showed a very high coefficient of determination ($R^2$ of 0.98) between homologous bands [18]. Moreover, the comparison of an automated approach for burned areas mapping combining OLI and MSI data, preprocessed rigorously, showed that both sensors have identified similarly the spatial patterns for burned areas [87 ].

Fig 10. Compared SSSI (a) and SEPM (b) derived from Sentinel-MSI and Landsat-OLI images data acquired in August 2017.

TABLE V. Regression fit equations between MSI and OLI image surface reflectance in the homologous spectral bands, and the derived SSSI and SEPM

## IV. CONCLUSIONS

The MSI onboard Sentinel satellites and the OLI installed on Landsat-8 satellite are designed to be similar in the perspective that their data be used together to support global Earth surface reflectance coverage for science and development applications at medium spatial resolution and near daily temporal resolution. However, relative spectral response profiles characterizing the filters responsivities of the both instruments are not identical between the homologous bands, so some differences are probably expected in the recorded land-surface reflectance values. This paper analyses and compares the difference between the reflectance of the homologous spectral bands in the VNIR and SWIR of MSI and OLI sensors for soil salinity dynamic monitoring in arid landscapes. In addition, comparisons were carried out in term of conversion of these surface reflectance to the SSSI and in term of the SEPM for salt-affected soil mapping. To achieve these, analyses were performed on simulated data and on two pairs of images acquired over the same area in July 2015 and August 2017 with one day difference between each pair. For simulated data, a field campaign was organized and 160 soil samples were collected with various degrees of soil salinity classes (i.e., extreme, very high, high, moderate, low, and non-saline). The bidirectional reflectance factor was measured above each soil sample in a Goniometric-Laboratory using an ASD spectroradiometer. Then, these measurements were resampled and convolved in the solar-reflective bands of SMI and OLI using the CAM5S TRC and the relative spectral response profiles characterizing the filters of these instruments. Furthermore, the used pairs of images were not cloudy, or cirrus contaminated, and without shadow effects. They were radiometrically and atmospherically corrected, and the differences related to BRDF were normalized. To generate data for analysis, similarly to OLI, MSI images were resampled systematically in 30 m by 30 m pixel size considering UTM projection and WGS84 datum. The comparisons of the surface reflectance, and derived SSSI and SEPM were undertaken in the same way for simulated and images data using regression analysis, $R^2$, and RMSD. The results obtained demonstrate that the statistical fits between SMI and OLI simulated surface reflectance over a wide range of soil samples with different salinity degrees reveals an excellent linear relationship ($R^2$ of 0.99) for all bands, as well as for SSSI and SEPM. The RMSD values are null between the NIR and SWIR homologous bands, and are insignificant for the other bands (i.e., 0.003 for coastal and 0.001 for the blue, green, and red bands). Moreover, the SSSI show an RMSD of 0.0007 and the SEPM express an excellent RMSD around 0.5 $dS.m^{-1}$ (electrical conductivity unit) reflecting a relative error that varies between 0.001 and 0.05, respectively, for salinity classes varying between 2.5 and 600 $dS.m^{-1}$. Likewise, the two used pairs of images exhibited very significant fits ($R^2$ of 0.93 for the costal and $R^2 \geq 0.96$ for the other bands of land surface reflectance, and $R^2$ of 0.95 for SSSI and SEPM). Excellent consistency was also observed between the derived products of the two sensors, yielding a RMSD values less than 0.029 (reflectance units) for the bands and less than 0.004 for SSSI. While, the calculated RMSD for the SEPM fluctuate between 0.12 and 2.65 $dS.m^{-1}$, respectively, of non-saline and extreme salinity classes, which means that the relative errors varies between 0.005 and 0.03 for the considered soil salinity classes (i.e., between non-saline to extreme salinity). In general, independently to the used data (simulated or images) the statistical fits found to be highly significant ($0.95 \leq R^2$) and the reached RMSD values (< 0.029) where smaller than the accuracy of radiometric calibration process (0.03) as demonstrated by Markham *et al.* [7]. Moreover, despite the small differences especially in coastal and blue bands, the results of this research pointed out that MSI and OLI sensors can be combined for high temporal frequency to monitor soil salinity dynamic in time and space in an arid landscape. However, rigorous preprocessing issues such as sensors calibration, atmospheric corrections, and BRDF normalisation must be addressed before the joint use of acquired data with these two sensors.

## V. ACKNOLEDGMENTS

The authors would like to thank the Arabian Gulf University (Kingdom of Bahrain) and United Arab Emirates University (United Arab Emirates) for their financial support. The NASA-USGS and ESA are thanked for the Landsat-OLI and Sentinel-MSI free data. Our gratitude to the anonymous reviewers for their constructive comments.

## VI. REFERENCES

[1] A. Dai, “Drought under Global Warming: A Review”. *WIREs Climate Change*, vol. 2, pp. 45–65, January / February 2011. DOI: 10.1002/wcc.81

[2] B. Kurylyk, and K. MacQuarrie, “The Uncertainty Associated with Estimating Future Groundwater Recharge: A Summary of Recent Research and an Example from a Small Unconfined Aquifer in a Northern Humid-Continental Climate”. *J. of Hydrology*, vol. 492, pp. 244-253, 2013.

[3] S. Shahid, and A. Al-Shankiti, “Sustainable Food Production in Marginal Lands-Case of GDLA Member Countries”. *Int. Soil and Water Conservation Research*, vol. 1, no. 1, pp. 24-38, 2013.

[4] S. Teh, and H. Koh, “Climate Change and Soil Salinization: Impact on Agriculture, Water and Food Security”. *Int. J. of Agriculture, Forestry and Plantation*, vol. 2, pp. 1-9, 2016.

[5] O.A. Naing *et al.* “Food Security and Socio-economic Impacts of Soil Salinization in Northeast Thailand”. *Int. J. of Environmental and Rural Development*, vol. 4, no. 2, pp. 76-81, 2013.

[6] R. White et al. “An Ecosystem Approach to Drylands: Building Support for New Development Policies”. Information Policy Brief, no.1, Washington DC, USA: World Research Institute, pp. 1-14, 2002.

[7] FAO “Management of Irrigation-Induced Salt-affected Soils”. Rome, Italy, 2005. [Online]. Available: http://www.fao.org/tempref/agl/agll/docs/salinity_brochure_eng.pdf

[8] G.I. Metternicht, and J.A. Zinck, “Remote sensing of soil salinity: Potentials and constraints”. *Remote Sens.of Env.*, vol. *85*, 1–20, 2003. DOI: 10.1016/S0034-4257(02)00188-8

[9] H. Zhang, J.L. Schroder, J.J. Pittman, J.J. Wang, and M.E. Payton, “Soil Salinity Using Saturated Paste and 1:1 Soil to Water Extracts”. *Soil Sci. Soc. Am. J.*, vol. *69*, pp. 1146–1151, 2005.

[10] G.I. Metternicht, and J.A. Zinck, “Spatial discrimination of salt- and sodium-affected soil surfaces”. *Int. J. Remote Sens.*, vol. 18, pp. 2571–2586, 1997.

[11] R. Goosens, M. El Badawi, and T. Ghabour, “De Dapper, M. A simulated model to monitor the soil salinity in irrigated arable land in arid areas based upon remote sensing and GIS”. *EARSeL Adv. Remote Sens.*, vol. *2*, pp. 165–171, 1998.

[12] A. Bannari, “Synergy Between Sentinel-MSI and Landsat-OLI to Support High Temporal Frequency for Soil Salinity Monitoring in an Arid Landscape”. Chapter 3 (pp. 67-93) in: Research Developments in Saline Agriculture, edited by Jagdish Chander Dagar, Rajender Kumar Yadav, and Parbodh Chander Sharma. Published by Springer Nature Singapore Pte Ltd. 2019, ISBN: 978-981-13-5831-9. DOI: 10.1007/978-981-13-5832-6. https://doi.org/10.1007/978-981-13-5832-6_3

[13] A. Abuelgasim, and R. Ammad, “Mapping soil salinity in arid and semi-arid regions using Landsat-8 OLI satellite data”. *Remote Sensing Applications: Society and Environment*, vol. 13, pp. 425-425, 2018. https://doi.org/10.1016/j.rsase.2018.12.010.

[14] A, Bannari, A. El-Battay, R. Bannari, and H. Rhinane, “Sentinel-MSI VNIR and SWIR Bands Sensitivity Analysis for Soil Salinity Discrimination in an Arid Landscape”. *Remote Sens.*, 10, 855, 2018. DOI:10.3390/rs10060855.

[15] E. Ben-Dor, M. Metternicht, N. Goldshleger, E. Mor, V. Mirlas, and U. Basson, “Review of Remote Sensing-Based Methods to Assess Soil Salinity”. Chapter 13, pp. 39–60 In *Remote Sensing of Soil Salinization: Impact on Land Management*; G. Metternicht and J.A. Zinck, Eds.; CRC Press Taylor and Francis Group: Boca Raton, FL, USA, 2009.

[16] S. Nawar, H. Buddenbaum, J. Hill, and J. Kozak, "Modeling and Mapping of Soil Salinity with Reflectance Spectroscopy and Landsat Data Using Two Quantitative Methods (PLSR and MARS)". *Remote Sens.*, vol. *6*, pp. 10813–10834, 2014.

[17] J.A. Zinck, "Monitoring soil salinity from remote sensing data". *In Proc. of the 1st Workshop EARSel Special Interest Group on Remote Sensing for Developing Countries*, Gent, Belgium, 13–15 September 2000; pp. 359–368.

[18] E. Mandanici, and G. Bitelli, "Preliminary Comparison of Sentinel-2 and Landsat 8 Imagery for a Combined Use". *Remote Sens.*, 8, 1014, 2016. DOI:10.3390/rs8121014

[19] D.P. Roy et al. "Landsat-8: science and product vision for terrestrial global change research". *Remote Sens. of Env.*, vol. 145, pp. 154–172, 2014. https://doi.org/10.1016/j.rse.2014.02.001

[20] M.A. Wulder, T. Hilker, J.C. White, N.C. Coops, J.G. Masek, D. Pflugmacher, and Y. Crevier, "Virtual constellations for global terrestrial monitoring". *Remote Sens. of Env.*, vol. 170, pp. 62–76, 2015. https://doi.org/10.1016/j.rse.2015.09.001

[21] H.K. Zhang, D.P. Roy, L. Yan, Z. Li, H. Huang, E. Vermote, S. Skakun, and J.C. Roger, "Characterization of Sentinel-2A and Landsat-8 top of atmosphere, surface, and nadir BRDF adjusted reflectance and NDVI differences". *Remote Sens. of Env.*, vol. 215, pp. 482-494, 15th September 2018. https://doi.org/10.1016/j.rse.2018.04.031

[22] J. Hedley, C. Roelfsema, B. Koetz, and S. Phinn, "Capability of the Sentinel 2 mission for tropical coral reef mapping and coral bleaching detection". *Remote Sens. of Env.*, vol. 120, pp. 145–155, 15th May 2012. https://doi.org/10.1016/j.rse.2011.06.028

[23] J. Li, and D.P. Roy, "A Global Analysis of Sentinel-2A, Sentinel-2B and Landsat-8 Data Revisit Intervals and Implications for Terrestrial Monitoring". *Remote Sens.*, 9, 902, 2017. DOI: 10.3390/rs9090902.

[24] M. Drusch, U. Del-Bello, S. Carlier, O. Colin, V. Fernandez, F. Gascon, B. Hoersch, et al. "Sentinel-2: ESA's optical high-resolution mission for GMES operational services". *Remote Sens. of Env.*, vol. 120, pp. 25–36, 15th May 2012. https://doi.org/10.1016/j.rse.2011.11.026

[25] J.R. Irons, J.L. Dwyer, and J.A. Barsi, "The next Landsat satellite: the Landsat data continuity mission". *Remote Sens. of Env.*, vol. 122, pp. 11–21, July 2012. https://doi.org/10.1016/j.rse.2011.08.026

[26] N. Flood, "Comparing Sentinel-2A and Landsat 7 and 8 Using Surface Reflectance over Australia". *Remote Sens.*, 9, 659, 2017. DOI: 10.3390/rs9070659.

[27] B. Markham et al. "Landsat-8 operational land imager radiometric calibration and stability". *Remote Sens*., vol. 6, no. 12, pp. 12275–12308, 2014.

[28] E.F. Vermote, C. Justice, M. Claverie, and B. Franch, "Preliminary analysis of the performance of the Landsat 8/OLI land surface reflectance product". *Remote Sens. of Env.*, vol. 185, pp. 46–56, November 2016. https://doi.org/10.1016/j.rse.2016.04.008

[29] D.P. Roy, J. Li, H.K. Zhang, L. Yan, H. Huang, and Z. Li, "Examination of Sentinel-2A multi-spectral instrument (MSI) reflectance anisotropy and the suitability of a general method to normalize MSI reflectance to nadir BRDF adjusted reflectance". *Remote Sens. of Env.*, vol. 199, pp. 25–38, 15th September 2017. https://doi.org/10.1016/j.rse.2017.06.019

[30] S. Skakun, J.C. Roger, E.F. Vermote, J.G. Masek, C.O. Justice, "Automatic subpixel co-registration of Landsat-8 operational land imager and sentinel-2A multispectral instrument images using phase correlation and machine learning based mapping". *Int. J. Digital Earth*, pp. 1–17, 2017.

[31] L. Yan, D.P. Roy, Z. Li, H.K. Zhang, and H. Huang, "Sentinel-2A multi-temporal misregistration characterization and an orbit-based sub-pixel registration methodology". *Remote Sensing of Env.,* vol. 215, pp. 495-506, 15th September 2018. https://doi.org/10.1016/j.rse.2018.04.021

[32] A. Bannari, P.M. Teillet, et R. Landry, "Comparaison des réflectances des surfaces naturelles dans les bandes spectrales homologues des capteurs TM de Landsat-5 et TME+ de Landsat-7". *Revue Télédétection,* vol. 4, no. 3, pp. 263-275, 2004.

[33] H. Van-der-Werff, and F. Van-der-Meer, "Sentinel-2A MSI and Landsat 8 OLI Provide Data Continuity for Geological Remote Sensing". *Remote Sens.*, 8, 883, 2016. DOI:10.3390/rs8110883.

[34] R.P. Shrestha, "Relating soil electrical conductivity to remote sensing and other soil properties for assessing soil salinity in northeast Thailand". *Land Degrad. Dev.*, vol. 17, pp. 677–689, 2006.

[35] A. Bannari, A.M. Guedon, and A. El-Ghmari, "Mapping Slight and Moderate Saline Soils in Irrigated Agricultural Land Using Advanced Land Imager Sensor (EO-1) Data and Semi-Empirical Models". *Commun. Soil Sci. Plant Anal.*, vol. 47, pp. 1883–1906, 2016.

[36] A. Bannari, A. El-Battay, N. Hameid, and F. Tashtoush, "Salt-Affected Soil Mapping in an Arid Environment using Semi-Empirical Model and Landsat-OLI Data". *Adv. Remote Sens.*, vol. 6, pp. 260–291, 2017.

[37] A. Bannari, S.A. Shahid, A. El-Battay, A. Alshankiti, N.A. Hameid, and F. Tashtoush, "Potential of WorldView-3 data for Soil Salinity Modeling and Mapping in an Arid Environment". In Proc. of IGARSS-2017, Fort Worth, TX, USA, 23–28 July 2017; pp. 1585–1588.

[38] A.P. Leone, M. Menenti, A. Buondonno, A. Letizia, C. Maffei, and G. Sorrentino, "A field experiment on spectrometry of crop response to soil salinity". *Agric. Water Manag*., vol. 89, pp. 39–48, 2007.

[39] I.O.A. Odeh, and A. Onus, "Spatial analysis of soil salinity and soil structural stability in a semiarid region of New South Wales, Australia". *Environ. Manag*, vol. 42, pp. 265–278, 2008.

[40] T.T. Zhang, S.L. Zeng, Y. Gao, Z.T. Ouyang, B. Li, C.M. Fang, and B. Zhao, "Using hyperspectral vegetation indices as a roxy to monitor soil salinity". *Ecol. Indic.*, vol. 11, pp. 1552–1562, 2011. DOI:10.1016/j.ecolind.2011.03.025.

[41] J.E. Chapman, D.A. Rothery, P.W. Francis, and A. Pontual, "Remote sensing of evaporite mineral zonation in salt flats (salars)". *Int. J. Remote Sens.*, vol. 10, pp. 245–255, 1989. DOI:10.1080/01431168908903860.

[42] N.A. Drake, "Reflectance spectra of evaporite minerals (400–2500 nm): Applications for remote sensing". *Int. J. Remote Sens., 16*, 55–71, 1995. DOI:10.1080/01431169508954576

[43] F. Hawari, "Spectroscopy of evaporates". *Per. Miner.*, vol. 71, pp. 191–200, 2002.

[44] S. Nawar, H. Buddenbaum, and J. Hill, "Digital Mapping of Soil Properties Using Multivariate Statistical Analysis and ASTER Data in an Arid Region". *Remote Sens.*, vol. 7, pp. 1181–1205, 2015. DOI:10.3390/rs70201181.

[45] M. Rahmati, and N. Hamzehpour, "Quantitative remote sensing of soil electrical conductivity using ETM+ and ground measured data". *Int. J. Remote Sens.*, *38*, 123–140, 2017.

[46] Analytical Spectral Devices, ASD Inc., Technical Guide 4th edition, 1999. [Online] Available: http://www.asdi.com/products-spectroradiometers.asp.

[47] P.M. Teillet, and R. Santer, "Terrain Elevation and Sensor Altitude Dependence in a Semi-Analytical Atmospheric Code". *Can. J. Remote Sens.*, vol. 17, pp. 36–44, 1991.

[48] N.A. Elagib, and S.A.A. Abdu, "Climate variability and aridity in Bahrain". *J. Arid Env.*, vol. 36, pp. 405–419, 1997.

[49] FAO "Bahrain: Geography, Climate and Population", 2015. [Online] Available: http://www.fao.org/nr/water/aquastat/countries_regions/bahrain/index.stm.

[50] C. Boonthaiiwai, and P. Saenjan, "Food Security and Socio-economic Impacts of Soil Salinization in Northeast Thailand". *Int. J. Environ. Rural Dev.*, vol. *4*, pp. 76–81, 2013.

[51] USDA-NRCS, "Soil Survey Laboratory Methods Manual". Soil Survey Investigations Report, No. 42 Version 4; 736 pages; R. Burt Edithor; USDA-NRCS: Washington, DC, USA, 2004.

[52] D.B. Lobell and G.P., Asner, "Moisture effects on soil reflectance". Soil Science Society of America Journal, vol. 66, pp. 722–727, 2002.

[53] J. Farifteh, F. Van der Meer, M. Van der Meijde and C. Atzberger, "Spectral characteristics of salt-affected soils: A laboratory experiment". Geoderma, vol. 145, pp. 196–206, 2008.

[54] J.C. Doomkamp, D. Brunsden, and D.K.C. Jones, "Geology, Geomorphology and Pedology of Bahrain". Geo-Abstracts Ltd., University of East Anglia: Norwich, UK, 443 pages, 1980

[55] R.D. Jackson, P.J. Pinter, J. Paul, R.J. Reginato, J. Robert, and S.B. Idso, "Hand-Held Radiometry". Agricultural Reviews and Manuals, ARM-W-19; U.S. Department of Agriculture Science and Education Administration: Phoenix, AZ, USA, 1980.

[56] St. Sandmeier, Ch. Muller, B. Hosgood and G. Andreoli, "Sensitivity Analysis and quality Assessment of Laboratory BRDF Data". *Remote Sens. of Env.*, vol. 64, pp. 176–191, 1998.

[57] E. Ben-Dor, C. Ong and I.C. Lau, "Reflectance measurements of soils in the laboratory: Standards and protocols". *Geoderma*, vol. 245–246, pp. 112–124, 2015.

[58] A. Bannari, P.M. Teillet, and G. Richardson, "Nécessité de l'étalonnage radiométrique et standardisation des données de télédétection". *Journal Canadien de Télédétection*, vol. 25, pp. 45-59, 1999.

[59] P.M. Teillet, K. Staenz, and D.J. Williams, "Effects of Spectral, Spatial, and Radiometric Characteristics on Remote Sensing Vegetation Indices of Forested Regions". *Remote Sens. of Env.*, vol. 61, pp. 139-149, 1997.

[60] M.D. Steven, T.J. Malthus, F. Baret, H. Xu, and M.J. Chopping, Intercalibration of vegetation indices from different sensor systems. *Remote Sens. of Env.*, vol. 88, pp. 412–422, 2003.

[61] H.K. Zhang, and D.P. Roy, "Computationally inexpensive Landsat 8 operational land imager (OLI) pan-sharpening". *Remote Sens.*, 8 (3), 180, 2016.

[62] S. Li, S. Ganguly, J.L. Dungan, W.L. Wang, and R.R. Nemani, "Sentinel-2 MSI Radiometric Characterization and Cross-Calibration with Landsat-8 OLI". *Advances in Remote Sensing*, vol. 6, pp. 147-159, 2017. DOI : 10.4236/ars.2017.62011.

[63] M.A. Wulder et al. "Current status of Landsat program, science, and applications". *Remote Sens. of Env.*, vol. 225, pp. 127–147, May 2019. https://doi.org/10.1016/j.rse.2019.02.015.

[64] T.R. Loveland, and J.L. Dwyer, "Landsat: Building a strong future". *Remote Sens. of Env.*, vol. 122, pp. 22–29, July 2012. https://doi.org/10.1016/j.rse.2011.09.022.

[65] M.A. Wulder, J.C. White, T.R. Loveland, C.E. Woodcock, A.S. Belward, W.B. Cohen, E.A. Fosnight, J. Shaw, J.G. Masek, and D.P. Roy, "The global Landsat archive: Status, consolidation, and direction". *Remote Sens. of Env.*, vol. 185, pp 271-283, 2015. http://dx.doi.org/10.1016/j.rse.2015.11.032.

[66] D. Roy, H. Zhang, J. Ju, J. Gomez-Dans, P. Lewis, C. Schaaf, Q. Sun, J. Li, H. Huang, and V. Kovalskyy, "A general method to normalize Landsat reflectance data to nadir BRDF adjusted reflectance". *Remote Sens. of Env.*, vol. 176, pp. 255–271, April 2016. https://doi.org/10.1016/j.rse.2016.01.023.

[67] NASA "Landsat-8 Instruments", 2014. [Online] Available: http://www.nasa.gov/mission_pages/landsat/spacecraft/index.html.

[68] E.J. Knight, and G. Kvaran, "Landsat-8 Operational Land Imager Design, Characterization and Performance". *Remote Sens.*, vol. 6, pp. 10286-10305, 2014. DOI:10.3390/rs61110286.

[69] F. Gascon et al. "Copernicus sentinel-2 calibration and products validation status". *Remote Sens.*, 9, 584, 2017. https://doi.org/10.3390/rs9060584.

[70] A. Stumpf, D. Michéa, and J.-P. Malet, "Improved Co-Registration of Sentinel-2 and Landsat-8 Imagery for Earth Surface Motion Measurements". *Remote Sens.*, 10, 160, 2018. DOI: 10.3390/rs10020160

[71] R.B. Myneni, and G. Asrar, "Atmospheric Effects and Spectral Vegetation Indices". *Remote Sens. of Environ.*, vol. 17, pp. 390-402, 1994. https:/doi.org/10.1016/0034-4257(94)90106-6.

[72] N. Pahlevan, Z. Lee, J. Wei, C.B. Schaaf, J.R. Schott, and A. Berk, A. "On-Orbit Radiometric Characterization of OLI (Landsat-8) for Applications in Aquatic Remote Sensing". *Remote Sens. of Environ.*, vol. 154, pp. 272-284, 2014. https:/doi.org/10.1016/j.rse.2014.08.001.

[73] P.M. Teillet, "An Algorithm for the Radiometric and Atmospheric Correction of AVHRR Data in the Solar Reflective Channels". *Remote Sens. of Environ.*, vol. 41, pp. 185-195, 1992. https:/doi.org/10.1016/0034-4257(92)90077-W.

[74] J. Qi, "Compositing multitemporal remote sensing data". Ph.D dissertation, Department of Soil and Water Science, University of Arizona, Tucson, Arizona, USA, 200 pages, 1993..

[75] E. Scudiero, T.H. Skaggs, and D.L. Corwin, "Comparative regional-scale soil salinity assessment with near-ground apparent electrical conductivity and remote sensing canopy reflectance". *Ecol. Indic.*, vol. *70*, pp. 276–284, 2016.

[76] A. Bannari, A.M. Guedon, A. El-Harti, F.Z. Cherkaoui, and A. El-Ghmari, A. "Characterization of Slight and Moderate Saline and Sodic Soils in Irrigated Agricultural Land (Tadla, Morocco) Using Simulated Data of ALI (EO-1) Sensor". J. of Soil Science and Plant Analysis, vol. 39, pp. 2795-2811, 2008.

[77] X.W. Fan, Y.B. Liu, J.M. Tao, and Y.L. Weng, "Soil salinity retrieval from advanced multi-spectral sensor with partial least square regression". *Remote Sens.*, vol. *7*, pp. 488–511, 2015.

[78] D.D. Alexakis, I.N. Daliakopoulos, L.S. Panagea, and I.K. Tsanis, "Assessing soil salinity using WorldView-2 multispectral images in Timpaki, Crete, Greece". Geocarto International, vol. 33, Issue, 4, pp. 321-338, 2016. DOI: 10.1080/10106049.2016.1250826.

[79] A. El-Battay, A. Bannari, N.A. Hameid, and A.A. Abahussain, "Comparative Study among Different Semi-Empirical Models for Soil Salinity Prediction in an Arid Environment Using OLI Landsat-8 Data". *Adv. Remote Sens.*, vol. *6*, pp. 23–39, 2017.

[80] Z. Al-Ali, A. Bannari, N. Hameid, and A. El-Battay, "Physical Models for Soil Salinity Mapping over Arid Landscape using Landsat-OLI and Field-Soil Sampling data: Validation and Comparison". In Proc. of IGARSS, July 28th to August 2nd, 2019, Yokohama, Japan, pp. 7081-7084.

[81] H. Wu, and A. Li, "Scale Issues in Remote Sensing: A Review on Analysis, Processing and Modeling". *Sensors*, vol. 9, pp. 1768-1793, 2009. DOI:10.3390/s90301768.

[82] C.J. Willmott, "Some comments on the evaluation of model performance". *Bull. Am. Meteorol. Soc*., vol. 63, pp. 1309–1313, 1982.

[83] J.D. Rhoades, F. Chanduvi, and S. Lesch, "Soil salinity assessment: methods and interpretation of electrical conductivity measurements". FAO irrigation and drainage report No. 57, Rome, Italy. 165 pages, 1999. [Online] Available: http://www.fao.org/docrep/019/x2002e/x2002e.pdf

[84] E. Davis, C. Wang, and K. Dow, "Comparing Sentinel-2 MSI and Landsat 8 OLI in soil salinity detection: a case study of agricultural lands in coastal North Carolina". *Int. J. of Remote Sens.*, vol. 40, no. 16, pp. 6134-6153, 2019. DOI: 10.1080/01431161.2019.1587205.

[85] N.J. Pastick, B.K. Wylie, and Z. Wu, "Spatiotemporal Analysis of Landsat-8 and Sentinel-2 Data to Support Monitoring of Dryland Ecosystems". *Remote Sens.*, 10, 791, 2018. DOI: 10.3390/rs10050791.

[86] F. Vuolo, M. Żółtak, C. Pipitone, L. Zappa, H. Wenng, M. Immitzer, M. Weiss, F. Baret, and C. Atzberger, "Data service platform for Sentinel-2 surface reflectance and value-added products: System use and examples". *Remote Sens.*, 8, 938, 2016.

[87] D.P. Roy, H. Huang, L. Boschett, L. Giglio, L. Yan, H.H. Zhangb, and Z. Li, "Landsat-8 and Sentinel-2 burned area mapping - A combined sensor multi-temporal change detection approach". *Remote Sens. of Env.*, vol. 231, 111254, 2019. https://doi.org/10.1016/j.rse.2019.111254.

Professor A. Bannari received a B.Sc. in Surveying Engineering from the Agronomic Institute Hassan-II (Rabat, Morocco), a M.Sc. in Geomatic sciences from Laval University (Quebec, Canada), and a Ph.D. in remote sensing form Sherbrook University (Sherbrook, Canada), respectively, in 1987, 1989, and 1996. After his early retirement as a remote sensing professor from the University of Ottawa (Ottawa, Canada), he was acting as a chair of the Department of Geoinformatics at the Arabian Gulf University (AGU), Kingdom of Bahrain. He was a visiting scientist at SPAR Aerospace Limited (Montreal, Quebec), JPL-NASA (Pasadena, USA), and Canada Centre for Remote Sensing (Ottawa, Canada). He is the author of two books and more than 220 articles, and he supervised more than 58 graduate students. Currently, he is running a private company "*Space Pix-Map International Inc.*" for international scientific consultations in remote sensing and Geomatics (Ottawa, Canada).

Dr. N. Hameid Mohamed Musa received a B.Sc. degree in Geology from University of Mousl (Iraq) in 1988; a M.Sc. and a Ph.D. in Geoinformatics from University of Khartoum (Sudan) in 2006 and 2012, respectively. He worked during many years for ministry of Agriculture in Sudan for information technology integration in natural resource applications. Since 2001 he hold a Geoinformatics specialist position at the Arabian Gulf University in Kingdom of Bahrain.

Dr. A. Abuelgasim received both his masters and PhD degrees from Boston University in 1996. Following he worked for one year as an assistant professor of remote sensing and surveying at Sultan Qabous University in Oman. He later joined the NASA Goddard Space Flight Center in Maryland, USA in 1998 as a visiting scientist. In 2000 he relocated to Canada where he has been with the Canada Centre for Remote Sensing and the Canadian Space Agency as a research scientist. Dr. Abuelgasim is currently and associate professor with the department of Geography and Urban Sustainability, United Arab Emirates University, UAE. His research and teaching interests are focused on the analysis of geospatial data for information products generation, physical and human geography, hydrology, and on the effects of human induced environmental and ecological changes.

Dr. A. Elbattay got his B.Sc. in Environmental Studies from University Hassan-II (Mohammedia-Morocco) in 1998, his M.Sc. and PhD in Remote Sensing from INRS-Eau (Quebec, Canada) in 2001 and 2006, respectively. Actually he is a senior scientist – Remote Sensing and Drones Technology- at International Center for Biosaline Agriculture in Dubai (UAE). Concurrently, he is the Chief Innovation Officer at the first established and leading drones solutions company in Dubai; Falcon Eye Drones. Before that, Dr. Ali occupied assistant and associate professor positions, respectively, at the *Universiti Teknologi Malaysia* (Malaysia) and the Arabian Gulf University in Bahrain.

This article has been accepted for publication in a future issue of this journal, but has not been fully edited. Content may change prior to final publication. Citation information: DOI 10.1109/JSTARS.2020.2995543, IEEE Journal of Selected Topics in Applied Earth Observations and Remote Sensing

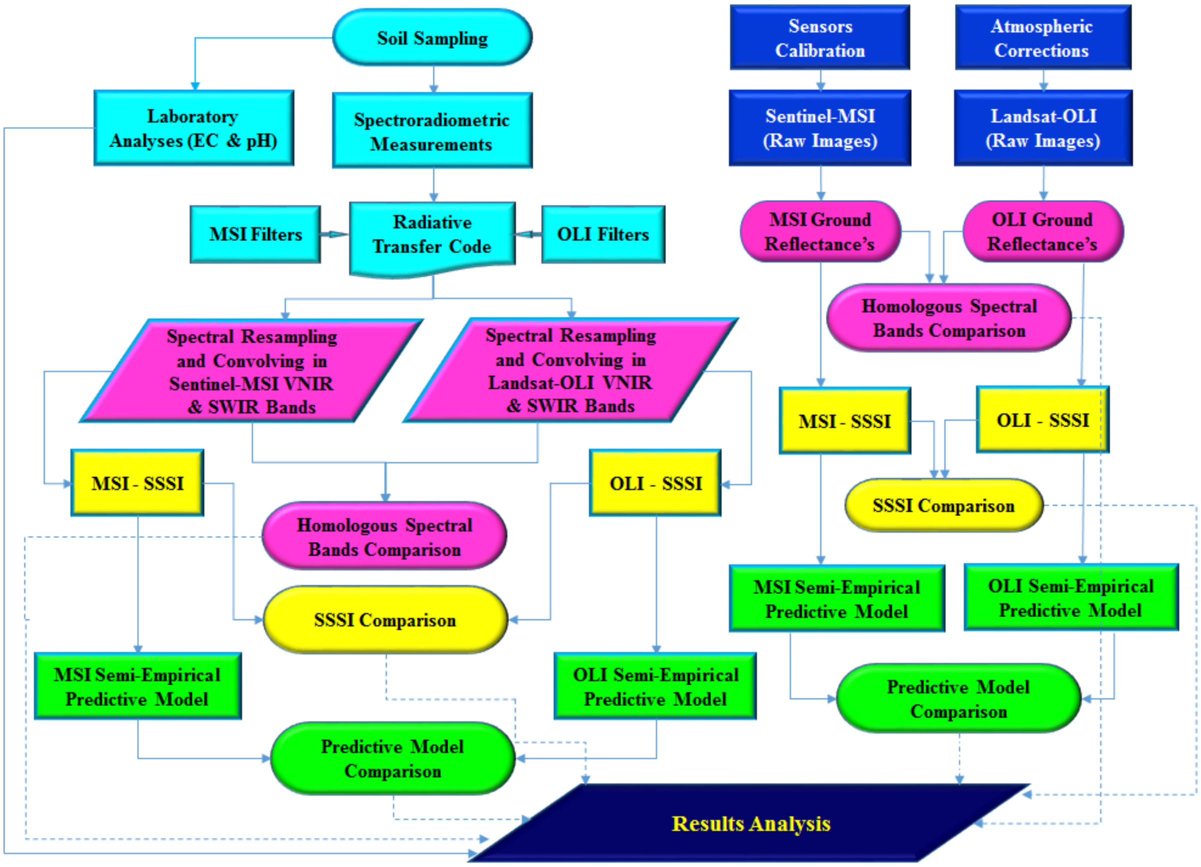

Fig 1. Flowchart of the methodology.

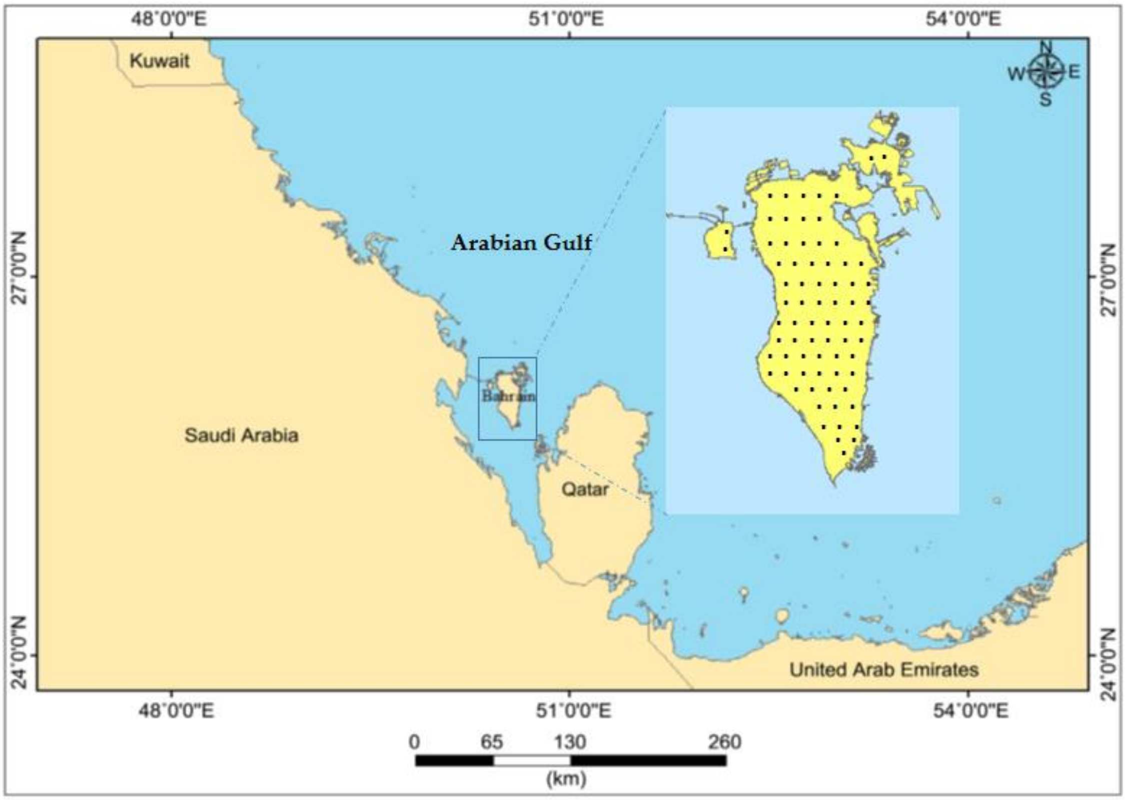

Fig 2. Study site (Kingdom of Bahrain).

Fig 3. Photos of the six considered soil salinity classes (C1 to C6).

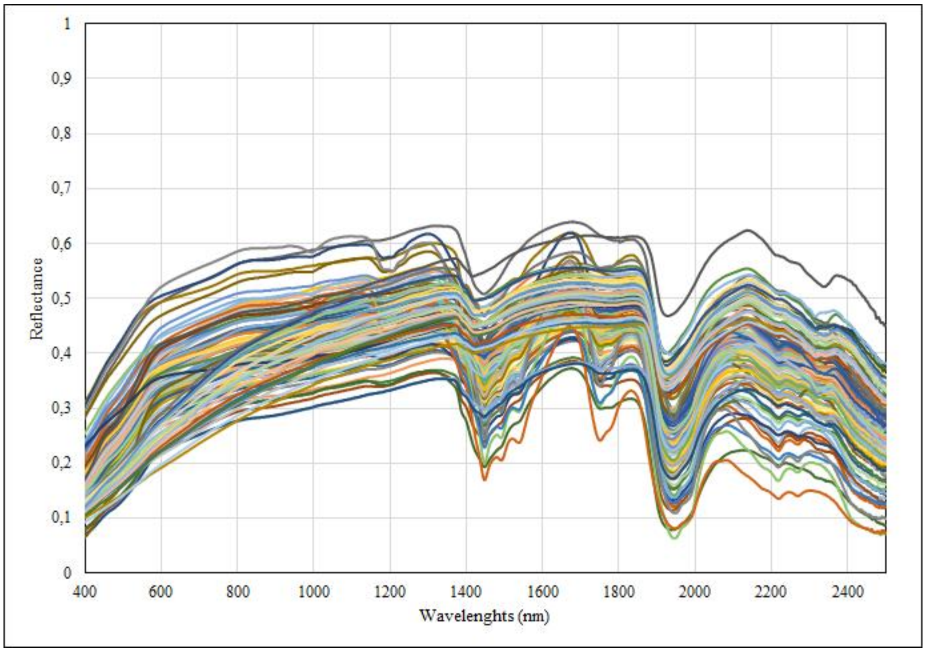

Fig 4. Spectral signatures of 160 soil samples with different degrees of salinity.

This article has been accepted for publication in a future issue of this journal, but has not been fully edited. Content may change prior to final publication. Citation information: DOI 10.1109/JSTARS.2020.2995543, IEEE Journal of Selected Topics in Applied Earth Observations and Remote Sensing

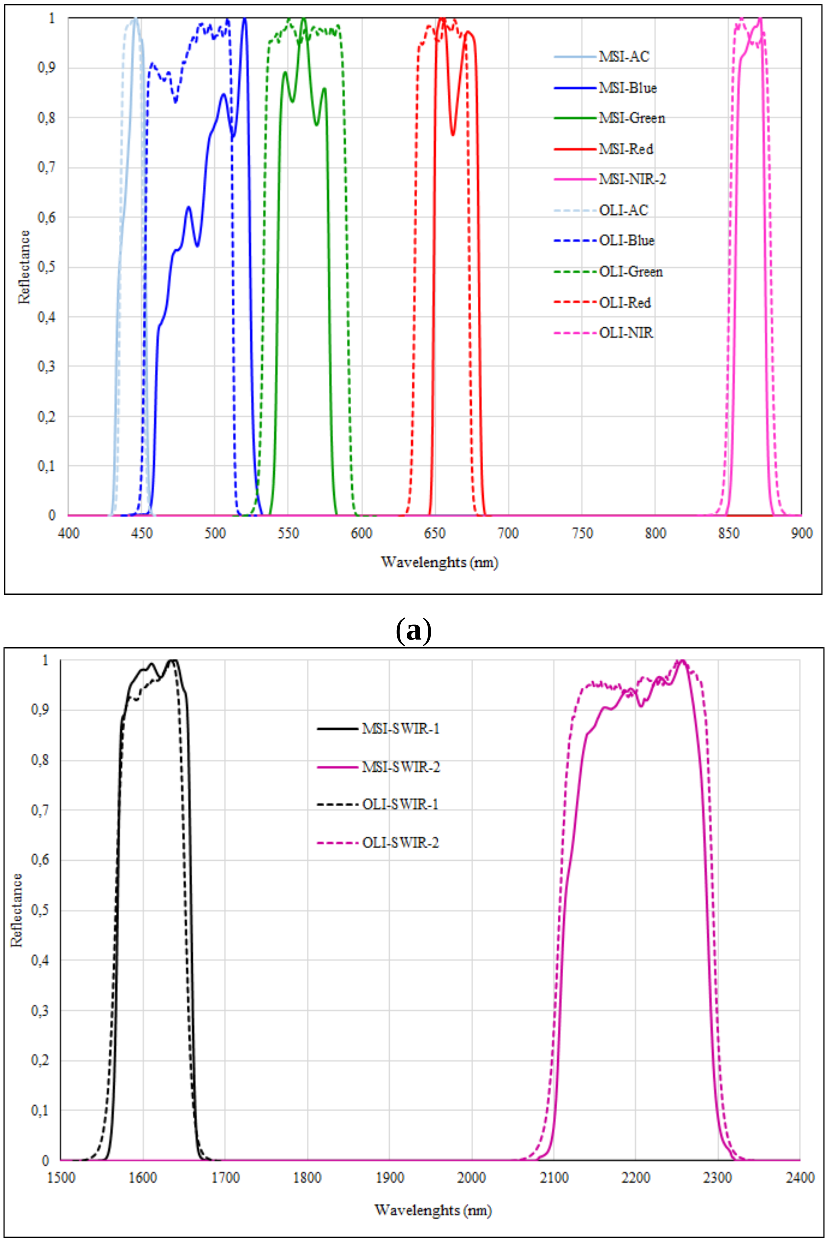

(**a**)

(**b**)

Fig 5. Sentinel-MSI and Landsat-OLI relative spectral response profiles characterizing the filters of each spectral band in the VNIR (a), and the SWIR (b).

This article has been accepted for publication in a future issue of this journal, but has not been fully edited. Content may change prior to final publication. Citation information: DOI 10.1109/JSTARS.2020.2995543, IEEE Journal of Selected Topics in Applied Earth Observations and Remote Sensing

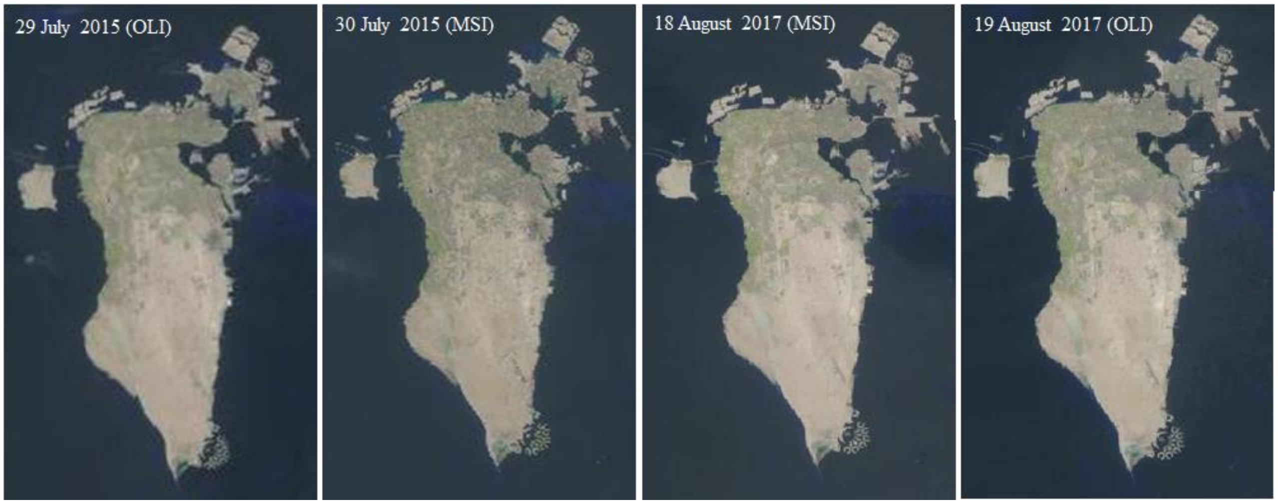

Fig 6. True color composite of raw OLI and MSI images data acquired over Kingdom of Bahrain in July 2015 (left) and August 2017 (right).

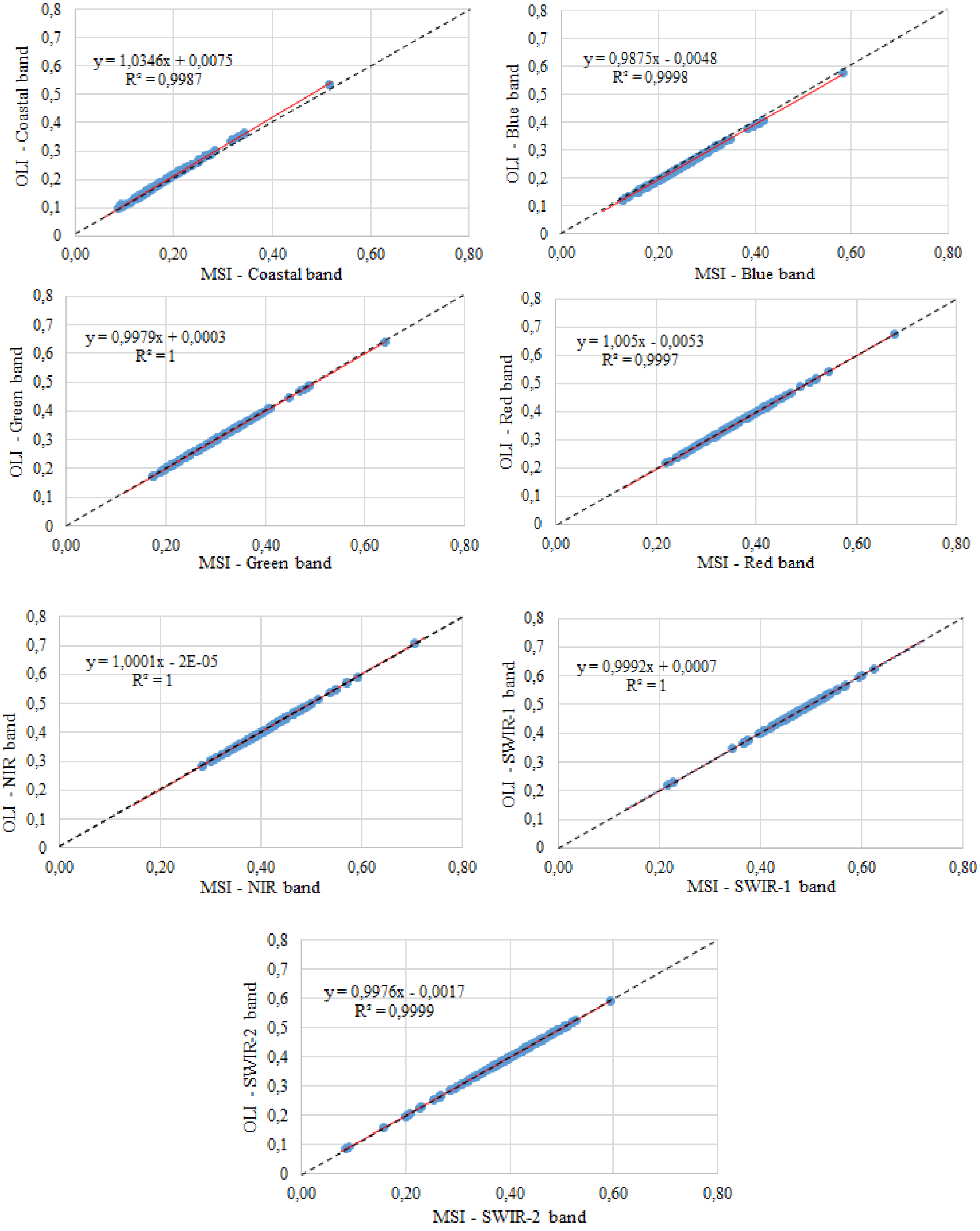

Fig 7. Compared surface reflectance simulated and convolved in Sentinel-MSI and Landsat-OLI homologous spectral bands.

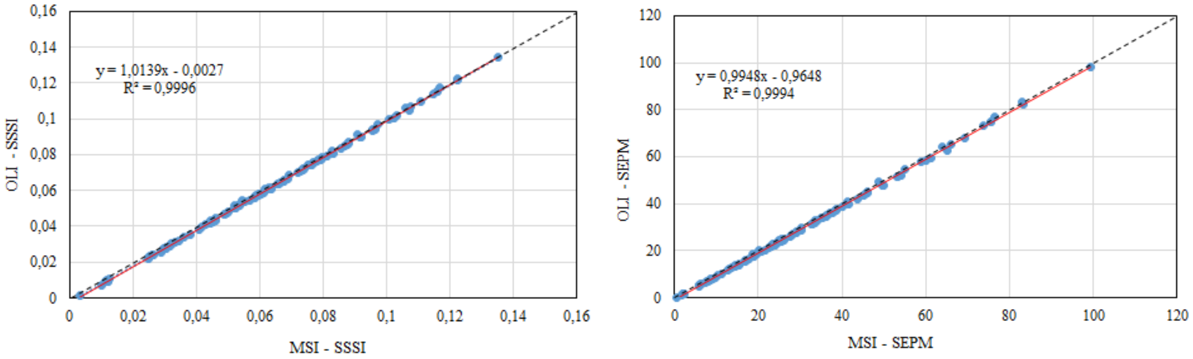

Fig 8. Compared SSSI (left) and SEPM (right) derived from Sentinel-MSI and Landsat-OLI simulated data.

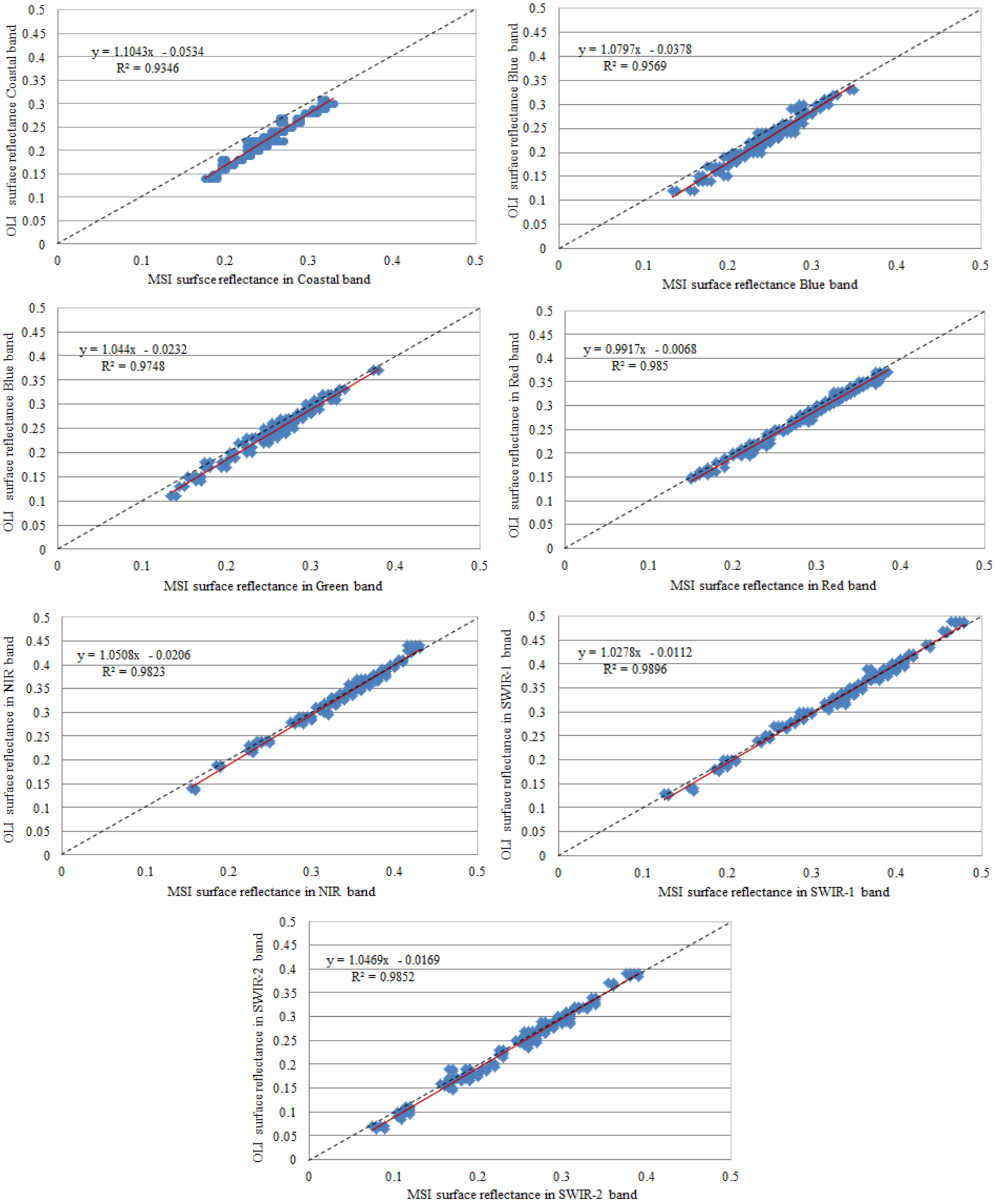

Fig 9. Compared surface reflectance acquired with Sentinel-MSI and Landsat-OLI spectral bands (VNIR and SWIR) acquired in August 2017.

This article has been accepted for publication in a future issue of this journal, but has not been fully edited. Content may change prior to final publication. Citation information: DOI 10.1109/JSTARS.2020.2995543, IEEE Journal of Selected Topics in Applied Earth Observations and Remote Sensing

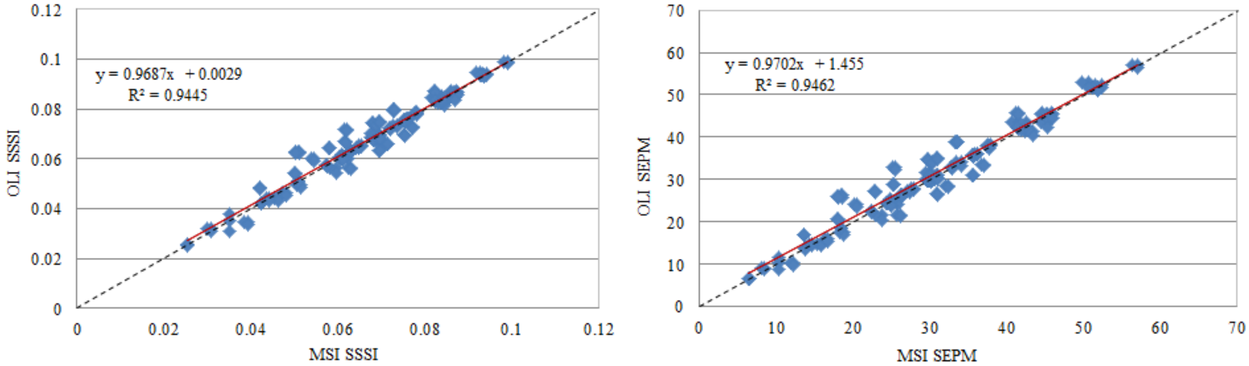

Fig 10. Compared SSSI (a) and SEPM (b) derived from Sentinel-MSI and Landsat-OLI images data acquired in August 2017.

TABLE I. The Sentinel-MSI and Landsat-OLI effective bandwidths and characteristics (λ = wavelength, SNR = signal to noise ratio).

| | Sentinel-MSI | | | | | Landsat-OLI | | | | |
|---|---|---|---|---|---|---|---|---|---|---|
| **Spectral Bands** | λ Centre (nm) | Δλ (nm) | Pixel Size (m) | SNR | $L_{ref}(\lambda)$ ($w/m^2/Sr/\mu m$) | λ Centre (nm) | Δλ (nm) | Pixel Size (m) | SNR | $E_0(\lambda)$ ($w/m^2/\mu m$) |
| Coastal | 443 | 20 | 60 | 129 | 129 | 443 | 16 | 30 | 130 | 1895.6 |
| Blue | 490 | 65 | 10 | 154 | 128 | 482 | 60 | 30 | 130 | 2004.6 |
| Green | 560 | 35 | 10 | 168 | 128 | 561 | 57 | 30 | 100 | 1820.7 |
| Red | 655 | 30 | 10 | 142 | 108 | 655 | 38 | 30 | 90 | 1549.4 |
| NIR-1 | 865 | 20 | 20 | 72 | 52.5 | 865 | 28 | 30 | 90 | 951.2 |
| SWIR-1 | 1609 | 85 | 20 | 100 | 4 | 1609 | 85 | 30 | 100 | 247.6 |
| SWIR-2 | 2201 | 187 | 20 | 100 | 1.5 | 2201 | 187 | 30 | 100 | 85.5 |

TABLE II. Input parameters for the CAM5S RTC (ASL: above sea level; GMT: Greenwich Mean Time; ppm: parts per million).

| **Parameters** | **MSI Images** | **OLI Images** |
|---|---|---|
| Terrain elevation (ASL) | 0.755 km | |
| Sensor elevation | 786 km | 705 km |
| Date of over-flight | 30 July 2015 | 29 July 2015 |
| Time of over-flight (GMT) | 10:22:47 | 10:04:19 |
| Solar zenith angle (deg.) | 20.201 | 23.811 |
| Solar azimuth angle (deg.) | 106.636 | 102.523 |
| Date of over-flight | 18 August 2017 | 19 August 2017 |
| Time of over-flight (GMT) | 10:20:33 | 10:04:46 |
| Solar zenith angle (deg.) | 22.516 | 26.010 |
| Solar azimuth angle (deg.) | 120.673 | 116.252 |
| Atmospheric model | Mid-latitude Summer | |
| Aerosol model | Continental | |
| Horizontal visibility | 50 km | 50 km |
| Ozone content | 0.319 cm-atm | |
| Water vapour | 2.93 $g/cm^2$ | |
| $CO_2$ mixing ratio | 357.5 ppm (as per model) | |

TABLE III. Laboratory determination of pH, EC-$_{\text{Lab}}$ and ions content in the different soil salinity classes.

| **Salinity class** | **EC-$_{\text{Lab}}$** (dS.m$^{-1}$) | **pH** | **Ca$^{2+}$** | **K$^{+}$** | **Mg$^{2+}$** | **Na$^{+}$** | **Cl$^{-}$** | **SO$_4^{2-}$** | **SAR** |
|---|---|---|---|---|---|---|---|---|---|
| | | | (mg.l$^{-1}$) | | | | | | **(mmoles/L)$^{0.5}$** |
| Extreme | 507.0 | 7.6 | 1276 | 843 | 672.0 | 154700 | 170715 | 11275 | 874.0 |
| V. high | 170.0 | 7.2 | 1878 | 1454 | 2874.0 | 76373 | 100281 | 28020 | 258.9 |
| High | 67.0 | 7.5 | 1905 | 651 | 1581.0 | 24171 | 48546 | 5488 | 99.2 |
| Moderate | 7.4 | 8.6 | 531 | 67 | 181.0 | 1324 | 2480 | 881 | 12.7 |
| Low | 4.4 | 8.2 | 284 | 44 | 96.0 | 782 | 1329 | 754 | 10.3 |
| Non-saline | 2.6 | 7.9 | 154 | 28 | 58.4 | 530 | 886 | 63 | 9.2 |

TABLE IV. Regression fit equations between MSI and OLI simulated surface reflectance in the homologous spectral bands, and the derived RMSD for SSSI and SEPM

| **Spectral Bands** | **Regressions between simulated data in OLI and MSI bands** | | |
|---|---|---|---|
| | Regression coefficients | R$^2$ | RMSD |
| Coastal | OLI = 1.0346 MSI + 0.0075 | 0.99 | 0.003 |
| Blue | OLI = 0.9875 MSI - 0.0048 | 0.99 | 0.001 |
| Green | OLI = 0.9979 MSI + 0.0003 | 1.00 | 0.001 |
| Red | OLI = 1.0050 MSI - 0.0053 | 1.00 | 0.001 |
| NIR-2 | OLI = 1.0001 MSI - 0.0002 | 1.00 | 0.000 |
| SWIR-1 | OLI = 0.9992 MSI + 0.0007 | 1.00 | 0.000 |
| SWIR-2 | OLI = 0.9976 MSI - 0.0017 | 1.00 | 0.000 |
| SSSI | OLI = 1.0139 MSI - 0.0027 | 1.00 | 0.0007 |
| SEPM | OLI = 0.9948 MSI - 0.9648 | 1.00 | 0.003 to 0.553* |

* dS.m$^{-1}$ for electrical conductivity unite; 0.003 dS.m-1 for non-saline and 0.553 for extreme salinity classes.

TABLE V. Regression fit equations between MSI and OLI image surface reflectance in the homologous spectral bands, and the derived RMSE for SSSI and SEPM

| | **Regressions between OLI and MSI for 2015** | | | **Regressions between OLI and MSI for 2017** | | |
|---|---|---|---|---|---|---|
| | Equations | R$^2$ | RMSD | Equations | R$^2$ | RMSD |
| Coastal | OLI = 0.8097 MSI + 0.009 | 0.94 | 0.026 | OLI = 1.1000 MSI + 0.050 | 0.93 | 0.029 |
| Blue | OLI = 1.1000 MSI + 0.048 | 0.96 | 0.021 | OLI = 1.0800 MSI + 0.040 | 0.96 | 0.021 |
| Green | OLI = 0.9241 MSI + 0.008 | 0.96 | 0.015 | OLI = 1.0400 MSI + 0.020 | 0.97 | 0.015 |
| Red | OLI = 0.9643 MSI + 0.004 | 0.98 | 0.015 | OLI = 0.9900 MSI + 0.010 | 0.98 | 0.011 |
| NIR | OLI = 1.0197 MSI + 0.019 | 0.99 | 0.010 | OLI = 1.0500 MSI + 0.020 | 0.98 | 0.009 |
| SWIR-1 | OLI = 0.9800 MSI + 0.000 | 0.99 | 0.010 | OLI = 1.0300 MSI + 0.010 | 0.99 | 0.008 |
| SWIR-2 | OLI = 1.0000 MSI + 0.000 | 0.99 | 0.007 | OLI = 1.0500 MSI + 0.020 | 0.99 | 0.008 |
| SSSI | OLI = 0.9839 MSI + 0.003 | 0.97 | 0.006 | OLI = 0.9700 MSI + 0.000 | 0.94 | 0.004 |
| SEPM * | OLI = 0.9352 MSI + 0.912 | 0.96 | 0.12 to 1.98 * | OLI = 0.9700 MSI + 1.460 | 0.95 | 0.12 to 2.65 * |

* dS.m$^{-1}$ for electrical conductivity unite; 0.12 dS.m-1 for non-saline and 2.65 for extreme salinity classes